Horizontal Single Belt Casting Process of AA2024. A Numerical and Physical Modelling Study

Justin Lee

Department of Mining and Materials Engineering

McGill University

Montreal, Canada

A thesis submitted to McGill University in partial fulfillment of the requirements for the degree of Master of Engineering

Abstract

Horizontal Single Belt Casting (HSBC) is an emerging Near Net Shape Casting process, for strip production. A thorough understanding of the heat, mass and fluid flow during casting process is necessary to determine the feasibility and quality of strip products in the production of aluminum alloys. In the following study, numerical and physical model studies were performed on the production of AA2024 using the HSBC process. A two-dimensional transient, turbulent CFD model was produced using ANSYS Fluent to evaluate the fluid flow and heat transfer during casting. The results were then experimentally validated using the HSBC simulator as well as the HSBC pilot scale system. From these, the interfacial heat flux values were calculated using Inverse Heat Conduction Problem (IHCP) methods. Macro and micro analyses on strip product, including surface quality, microstructure and porosity were evaluated. Top surface quality was shown to be dependent on both the Froude number and the velocity gradient at the interface, as determined by the Kelvin Helmholtz Instability. The following study concludes that the HSBC process can produce high quality AA2024 strips, given its improved interfacial heat fluxes and cast microstructure in comparison to traditional Direct Chill (DC) cast products.

Resumé

Le procédé de coulée continue à bande horizontale est un procédé innovant pour la production de bandes métalliques. Dans cette ètude, des modèles numériques de la mécanique des fluides et du transfert de chaleur ont été développés pour étudier la production de l'alliage AA2024 avec le procédé de coulée continue à bande horizontale. Des modèles deux dimensions et du turbulence avec les deux phases sont basés avec ANSYS Fluent et ont été validés avec des expériences du simulateur et du pilote. Des résultats pour les flux de chaleur sont déterminés avec la méthode IHCP. Les propriétés du macro et micro, y compris de la rugosité de surface, la microstructure et la porosité, ont été évaluées. Les résultats ont montré un flux de chaleur élevé et une bonne microstructure par rapport au la coulée en métal conventionnelle. Les résultats ont montré que la rugosité de la surface dépendait du nombre de Froude et l`instabilité de Kelvin-Helmholtz. La rugosité de la surface inférieure était similaire aux expériences précédentes en raison de l`évolution de l`entrefer. Cette étude conclut que le procédé de coulée continue à bande horizontale est une bonne alternative au la coulée en métal conventionnelle en raison des qualités des produits et le flux de chaleur élevé.

Acknowledgements

Through my two years as a Master`s student, I have learned from and worked alongside some incredible people, all of which have helped me complete my Master`s thesis. First, I would like to thank my supervisors, Professor R.I.L. Guthrie, Dr. Mihaiela Isac and Professor Mainul Hasan. From water modelling as a Co-op student at the McGill Metals Processing Centre (MMPC) to building numerical models and working with the pilot-scale HSBC machine, I am always learning and am always excited by the opportunities they have given me.

I want to express my deepest thanks to the MMPC team. Without the support of Dr. Luis Calzado, Usman Niaz, Jason Hsin, Mahdi Aboutalebi, Mianguang Xu, Carlos Riviere, Giacomo Di Silvestro, Samuel Filgueras Rodrigues, Ameth Maloum Fall, Ajay Panicker, Karim Selim and Shawn Zhu, the work and research presented in my Master's thesis would not have been possible. I am also incredibly grateful to NSERC and the supporting companies of the MMPC for their generous financial support.

Finally, I would like to thank my friends and family who supported my studies and my research over the last two years. You all helped keep a positive environment and for that, I am truly grateful.

Table of Contents

Table of Figures

Table of Tables

Introduction

With the current global requirements towards low cost, efficient and green technologies, the need for Near-Net-Shape Casting (NNSC) processes trends upwards. Strip casting in the aluminum industry remains a strong alternative to the traditional direct chill (DC) casting process, providing lower energy and capital costs and in turn lower production costs of strip products. By further integrating the casting process alongside in-line size reduction steps, one can obtain products of desired thicknesses without the need of reheating and additional hot rolling steps.

Aluminum alloy 2024 (AA2024) is a high strength aluminum alloy, primarily found in the aerospace industry. Offering excellent strength to weight ratio and fatigue resistance, the alloy is primarily used for structural components including wing's leading edges, engine cowlings, etc. During production, however, several casting concerns arise. These include hot cracking during casting, solidification and rolling. Due to the large freezing range (136 K), high solidification shrinkage, high coefficient of thermal expansion and segregation of alloying elements to the grain boundaries, there are casting concerns using DC casting.

This present study will investigate the casting of AA2024 using the Horizontal Single Belt Casting (HSBC) process. This is an emerging NNSC process offering both economic and environmental advantages to strip casting products. In addition, the HSBC additional provides high interfacial heat transfer rates and one directional freezing, both of which can mitigate hot cracking common in AA2024 casting [1, 2]. As such, the HSBC process is a promising alternative to produce a variety of aluminum, copper and steel strip products.

The following research that was conducted involves three primary objectives. First, to produce a turbulent, transient Computational Fluid Dynamics (CFD) and heat transfer model to predict fluid flow and heat transfer behaviour using the HSBC process. Second, to cast AA2024 using a simulator scale and pilot scale HSBC caster and third, to evaluate as-cast products, including surface quality, porosity and microstructures.

Chapter 1 Literature Review

1.1 Horizontal Single Belt Casting Development

The HSBC process was first independently conceived by Herbertson and Guthrie [1] and Reichelt, Schwerdtfeger and Voss-Spilker [3] both in 1988. Naturally, parallel development of the HSBC process began by both a European consortium and a North American consortium (led by Hazelett and McGill Metals Processing Centre). In 1999, a pilot-scale HSBC caster, initially located in Newcastle, Australia, was provided to the McGill Metals Processing Center (MMPC) in Montreal, Canada for further research and development. The HSBC pilot-scale system was upgraded significantly, thanks to a Canadian Foundation and Innovation (CFI) funding initiative and operated using a 600 lb induction furnace for melt preparations. A plunging metal displacement piston and a tundish/launder melt delivery system was designed, with associated pre-heating elements, to deliver the liquid aluminum alloy onto the 2.6 m long, water-cooled, textured steel belt. The melt solidifies onto the water-cooled belt, producing 1-10 mm thick as-cast strips at a belt speed of 24 m/min. A schematic of the HSBC pilot-scale caster is shown in Figure 1-1.

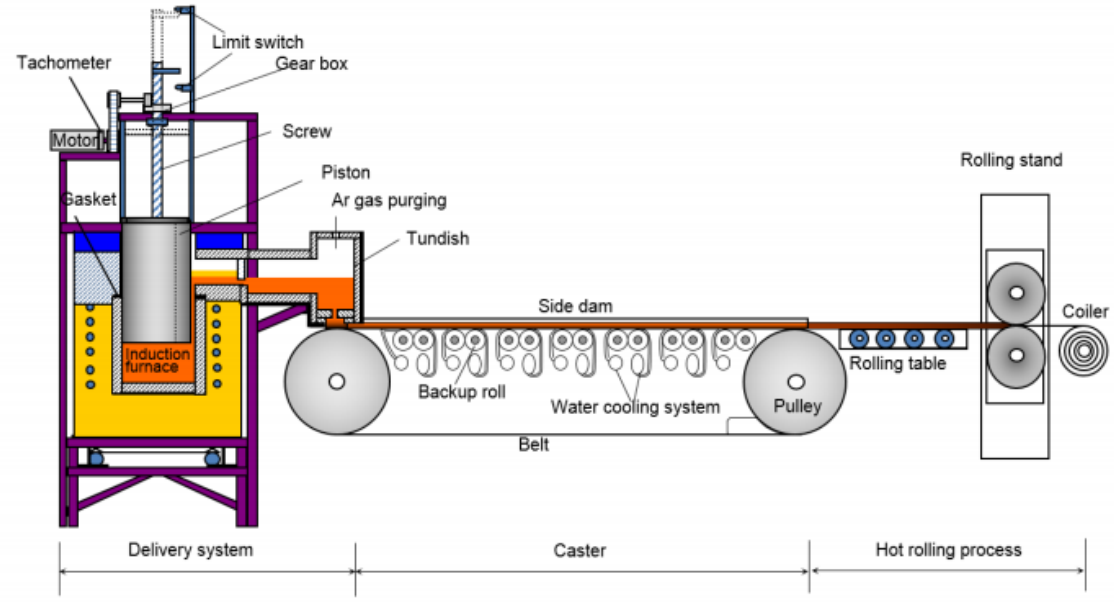

Figure 1-1 – Schematic of the HSBC Pilot Scale System [4]

At the MMPC, the pilot-scale caster and a smaller HSBC "simulator" was primarily used to evaluate belt substrate cooling and topography, and metal superheat effects, on the interfacial heat fluxes [2, 5-7], casting atmospheres [7, 8], and melt delivery systems [9-16]. A number of these delivery systems are shown in Figure 1-2. In addition, a variety of different alloy systems including steels [7, 17] and lower melting range crystalline alloys like aluminum [2, 5-8, 10, 13, 18-20], magnesium [21-23], and copper alloys, have all been studied by MMPC researchers.

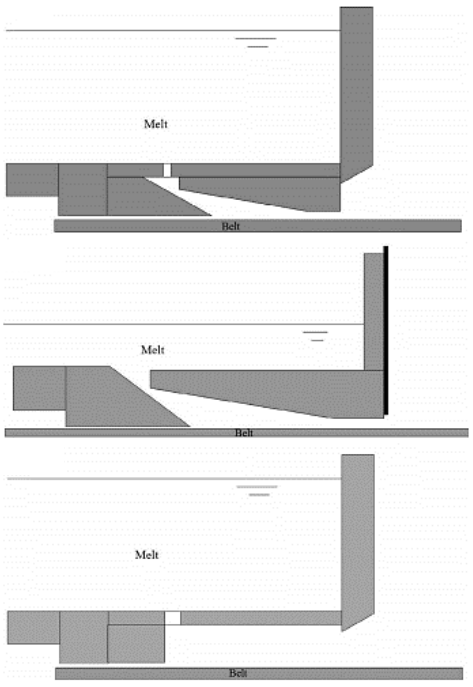

Figure 1-2 Delivery system configurations previously evaluated by the MMPC [11]

Significant research has focused on the development of CFD models of the HSBC in analyzing fluid flow and heat transfer behavior of the liquid melt. In addition, Inverse Heat Conduction Problem (IHCP) techniques have been used to determine interfacial heat flux behavior. Both will be discussed in detail in Chapter 1.4.

In the case of the TU Clausthal's Direct Strip Caster (DSC), a ladle/stopper rod system, as shown in Figure 1-3, is used to control the flow of metal into the launder system and onto the moving belt. Argon gas rakes are used to decelerate the liquid film and to evenly distribute liquid melt across the belt width, as the liquid metal first impacts the cooled belt with the water cooling system underneath. This is shown in Figure 1-3. This is followed by a shrouding system (argon and CO_2

mixture). An in-line rolling and downstream water quenching system allows for the appropriate size reduction, typically 50-80%, prior to cooling to the coiling temperature. Using the DSC system, it was shown in Figure 1-4 that the energy savings were reduced to 24% of those for Conventional Slab Casters (CSC) and 39% of those for Compact Strip Production (CSP).

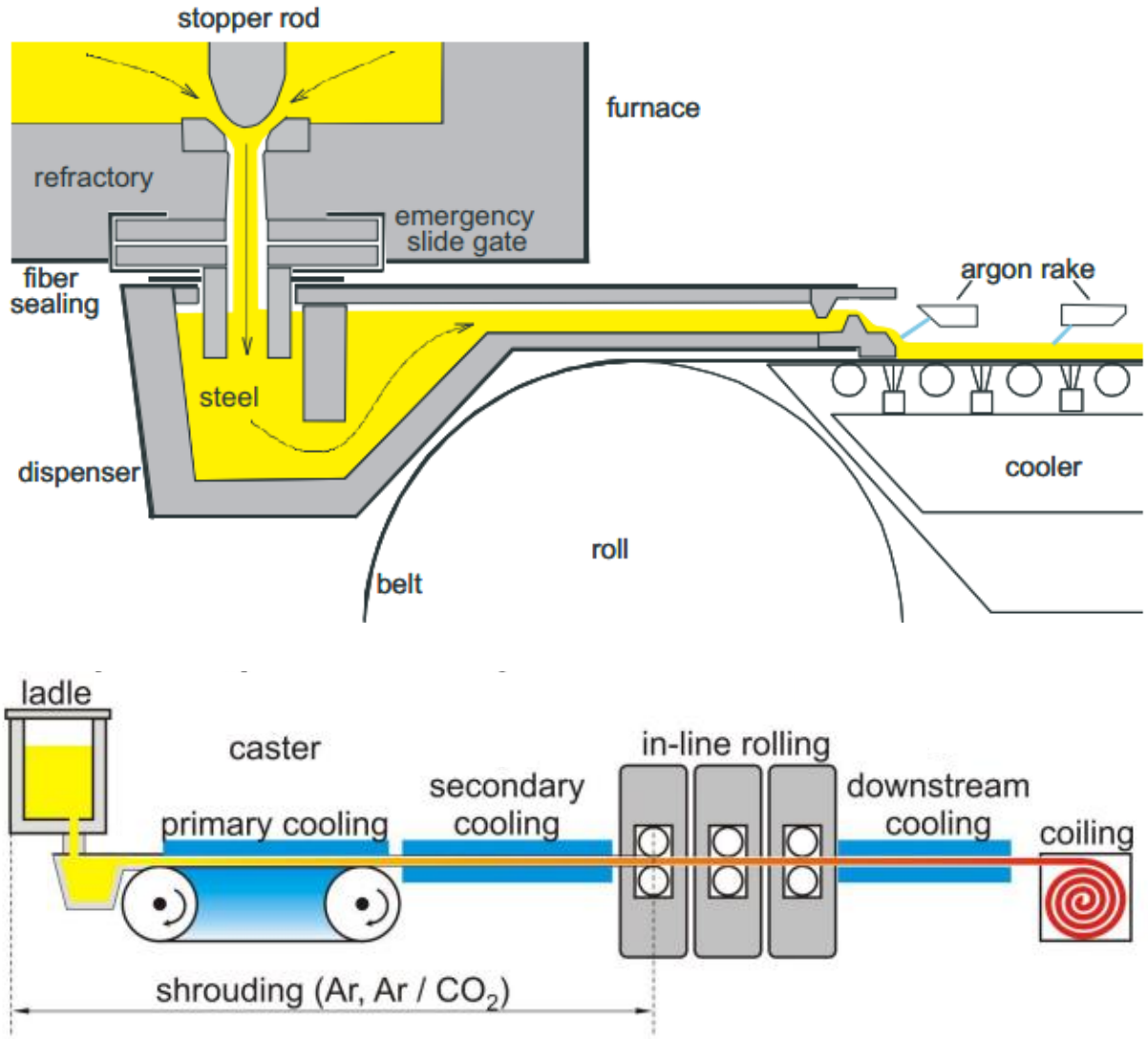

Figure 1-3 Schematic of the TU Clausthal HSBC ladle, launder and delivery system (Top) and full schematic of the TU Clausthal HSBC pilot-scale caster (Bottom) [24]

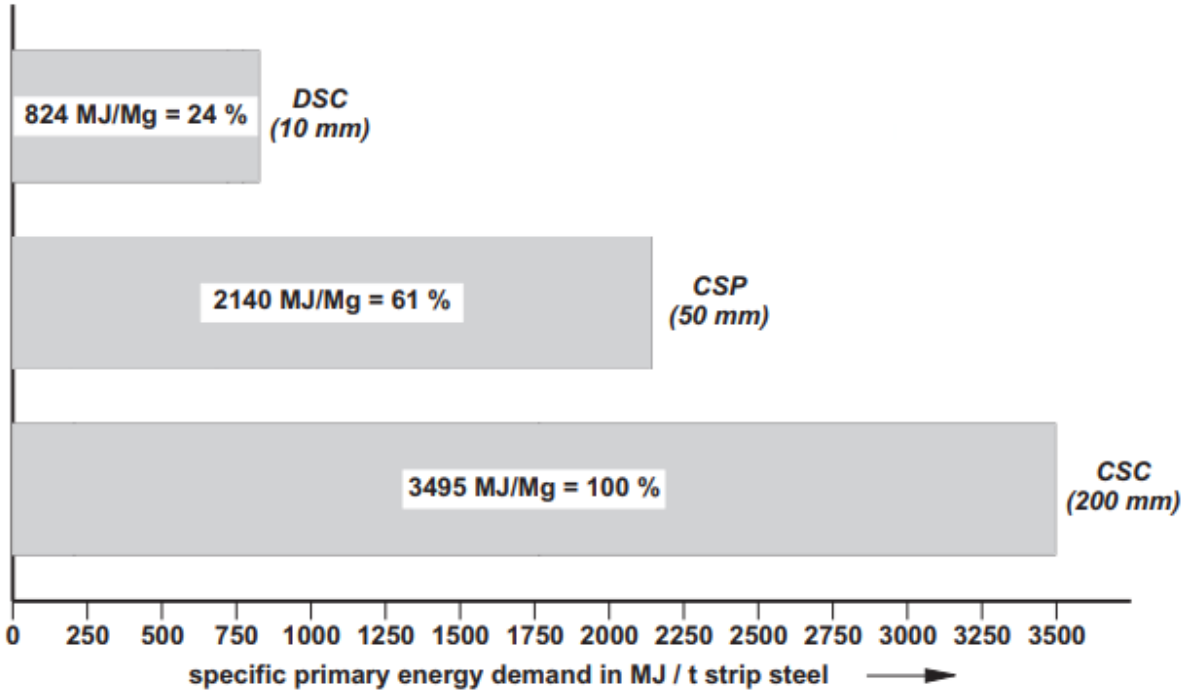

Figure 1-4 Energy savings in DSC in comparison to CSP and CSC machines [24]

1.2 Strip Properties of HSBC Products

Product quality is key in determining both the viability and advantage of the HSBC process in comparison to conventional continuous casting methods. One can describe strip properties in two categories. First are the macro-properties of the strip. Surface quality and edge quality fall under this category, as well as various cracking mechanisms. Second are the micro-properties of the strip. Microstructure, microsegregation and porosity are examples of micro-properties.

At the MMPC, both macro and micro-properties have been evaluated for strip products produced by the pilot-scale HSBC machine and the HSBC simulator-machine. Ge *et al.* produced Al-Mg-Sc-Zr alloys via the HSBC process and showed consistent surface quality between both the pilot-scale and simulator-scale HSBC machines [25]. Furthermore, analysis showed very small surface fluctuations for the top and bottom surface (85.1 μm and 41.9 μm respectively), with small protuberances appearing on the bottom surface. The 3-D profilometry analysis is shown in Figure 1-5.

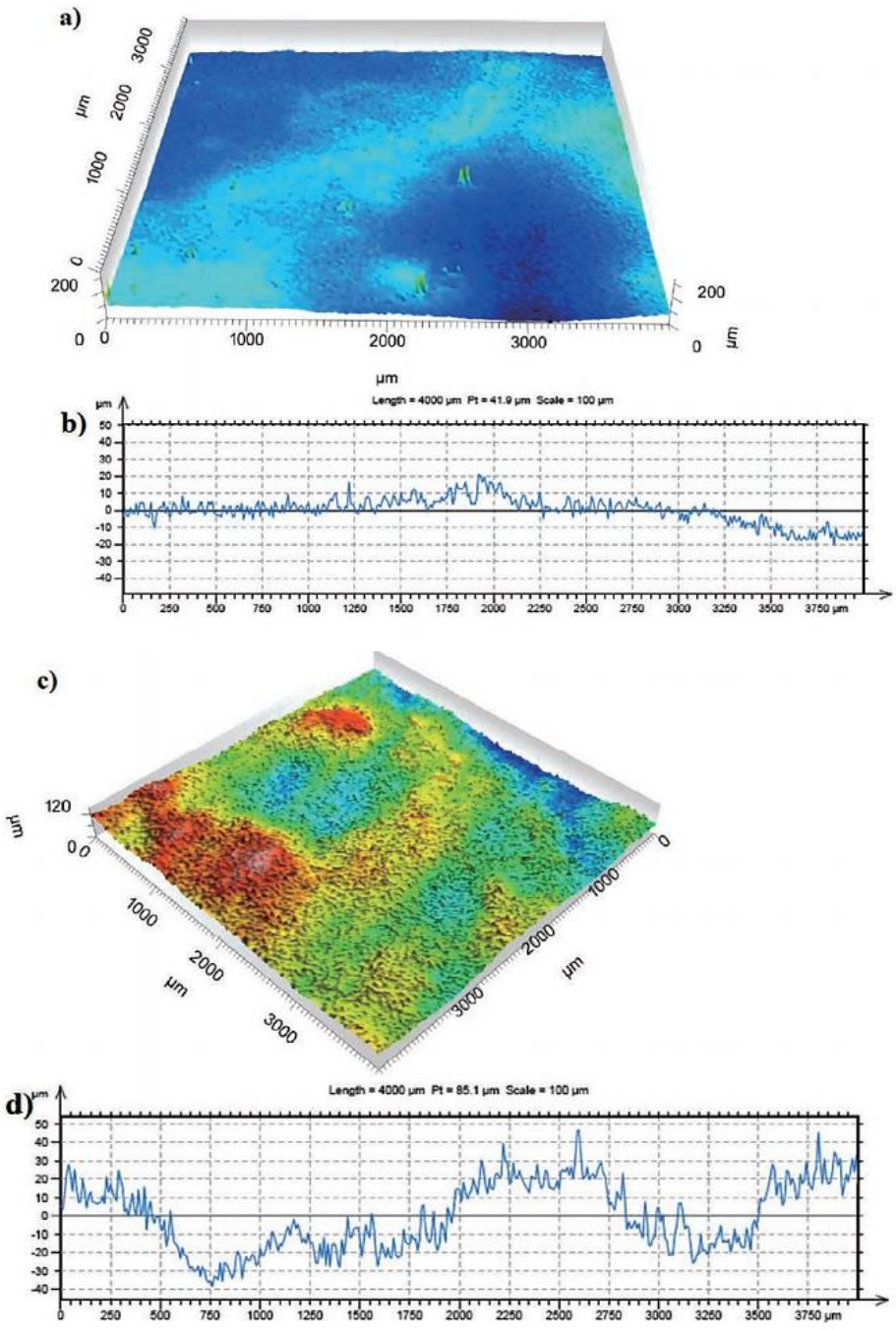

Figure 1-5 3D Surface Profilometry Analysis of HSBC produced Al-Mg-Sc-Zr alloy strips, a) bottom surface topography, b) bottom surface roughness analysis, c) top surface topography and d) top surface roughness analysis [25]

These small depressions have been analyzed thoroughly at the MMPC and it has been theorized that they are primarily caused by two phenomena (Figure 1-6). First, as the first points of contact between the liquid melt and the substrate (~169 points / mm^2), rapid heat transfer occurs and thus initiates solidified nuclei. Second is the formation of air gaps on the bottom surface of the melt, with the proposed mechanism shown in Figure 1-7.

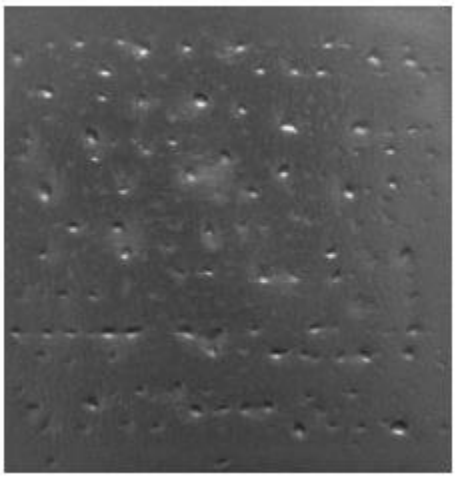

Figure 1-6 Surface depressions on the bottom surfaces of AA6111 HSBC strips, as produced by air entrapment and expansion within the peaks and valleys of the belt itself [7]

Several methods have been reviewed to mitigate the formation of these small protuberances on the bottom surface of the strip. Graphite spray coatings have previously been shown to not wet the aluminum melt, by weakening metal contact at the substrate interface [21, 26]. Due to the weakened interfaces between the melt and the belt surface, the increasing air pressure can be uniformly distributed across the bottom surface of the forming strip. Thus, whilst surface quality was shown to improve with a graphite coating, there can be a significant decrease in interfacial heat transfer measured, owing to the higher thermal resistance of the expanded air gap for the graphite coated surface of the belt. Second is the use of a textured substrate to reduce the entrapped air at the interface and thus improving surface quality and interfacial heat transfer. Using the macroscopically textured copper surfaces, Figure 1-8 (Left), allowed for a significantly increased interfacial heat flux in comparison to a sandblasted copper substrate with a graphite coating.

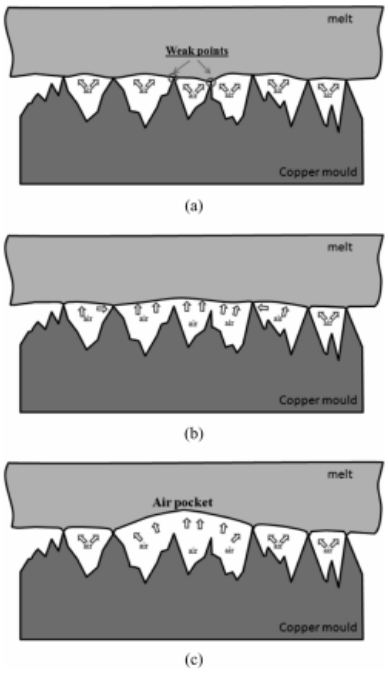

Figure 1-7 Proposed mechanism for the formation of depressions on the bottom surface of the melt. a) air entrapped underneath melt rapidly expand. b) due to gas expansion, melt loses contact with the substrate at the "weak points". c) air pocket formation leads to lower local heat extraction rates, delaying solidification and generation of depressions [2]

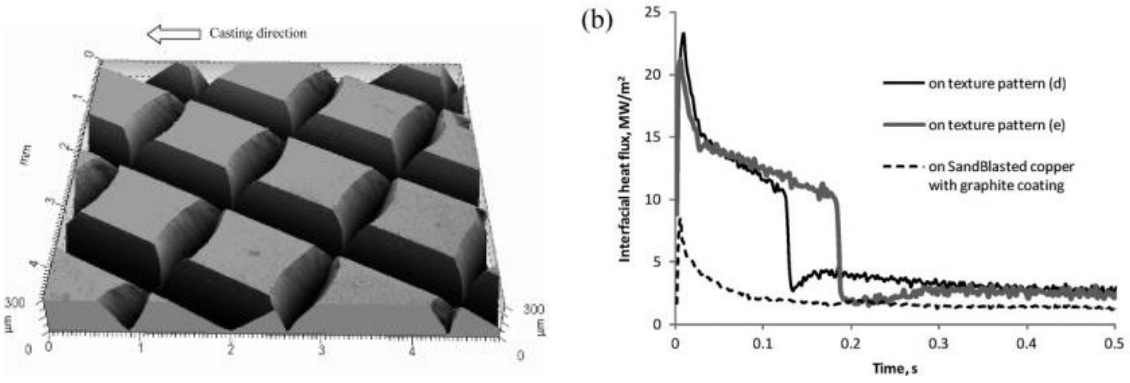

Figure 1-8 Surface topography of the macroscopically textured copper surface reviewed for the HSBC process (Left) and the interfacial heat fluxes using the textured surfaces (Right) [2]

Microstructural analysis was also performed on HSBC produced strips to evaluate the micro-properties. Due to the high cooling rates (of up to 500 K/s [11]), it is expected that the formation of the secondary phases remain present within the grains rather than the grain boundaries. As

shown by Ge *et al*., the secondary phases remained primarily within the grain rather than at the grain boundaries for ingot cast aluminum alloys [25]. This is shown more clearly in Figure 1-9, where a significant number of secondary phases exist near the grain boundaries for ingot cast samples.

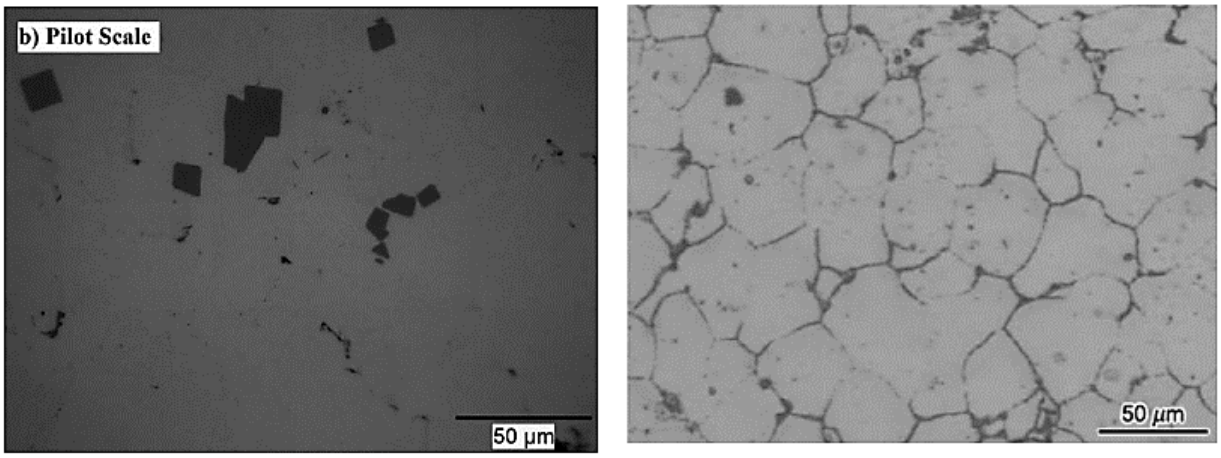

Figure 1-9 HSBC strip optical micrograph (left) [25] and ingot cast optical micrograph (right) [27]

Grain sizes for various textured surfaces and interfacial heat transfer rates were evaluated at the MMPC. Guthrie and Isac showed that textured copper surfaces, surface (d) and (e), resulted in smaller grain sizes in comparison to casting with a sand blasted, graphite coating sprayed substrate, as shown in Figure 1-10 [7]. The smaller grain sizes are due to the higher interfacial heat transfer rates shown in the use of pattern (d) and pattern (e) copper substrates, as shown in Figure 1-8. Furthermore, the grain sizes were shown to be smaller near the bottom of the strip, due to the higher heat transfer rates, in comparison to the bulk and the top of the strip.

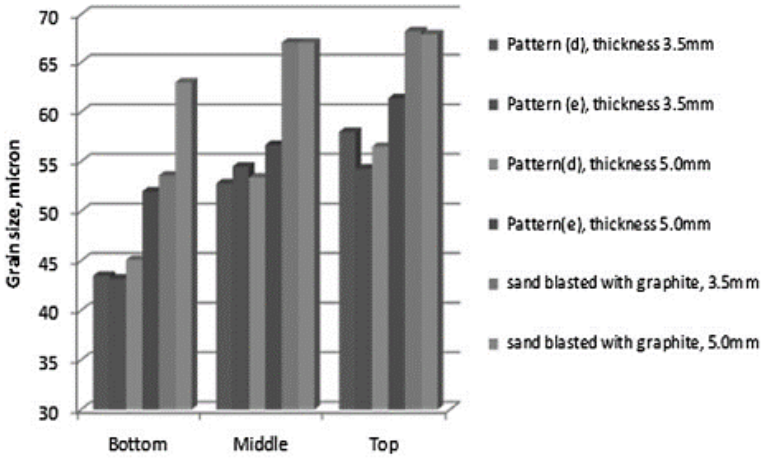

Figure 1-10 Grain size measurements for various substrate configurations for AA6111 strips produced by the HSBC simulator [7]

Secondary Dendrite Arm Spacing (SDAS) is also important in dictating the mechanical properties of the strip product. It was shown by Li *et al.* that with a higher cooling rate, the SDAS decreases, as shown in Figure 1-11 [26]. The relationship follows Equation (1), where t_f represents the solidification time (s) and SDAS in μm for AA6111.

$$SDAS = 11.5\left(t_f\right)^{0.43} \tag{1}$$

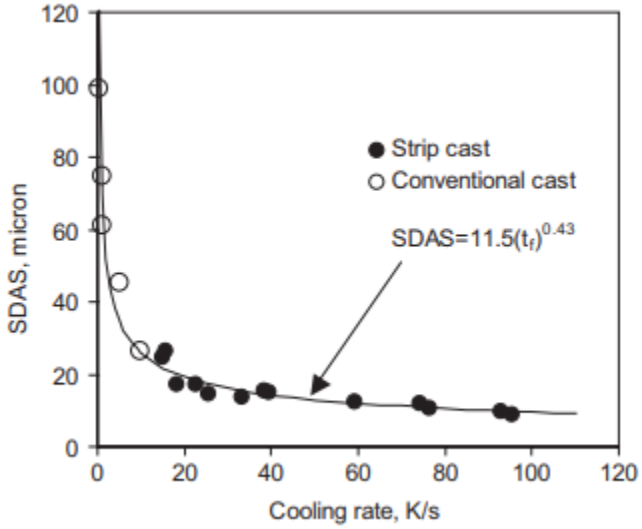

Figure 1-11 Relationship between cooling rate and SDAS for 2.5mm thick AA6111 strip [26]

1.3 AA2024 Mechanical Properties and Microstructure

The present study's primary focus is the casting of AA2024 strips using the HSBC process. To understand the primary advantage of using the HSBC process, one must first understand the material itself. Aluminum inherently has a high strength to weight ratio and thus is commonly used in the aerospace industry. AA2000 series, based on Al-Cu alloys, is commonly used due to the strength provided by solute copper. To understand its use, we must first look at the microstructure and how the various alloying elements found in AA2024 affect the microstructure. The composition of AA2024 is given in Table 1-1.

Table 1-1 Composition of AA2024 in Weight %

Al	Cu	Mn	Mg	Cr	Zn	Ti	Fe	Si	Other
Balance	3.8-4.9	0.3-0.9	1.2-1.8	0.1 max	0.25 max	0.15 max	0.5 max	0.5 max	0.15 max

Al-Cu Binary Phase Systems

The addition of copper allows for the precipitation hardening of the alloy through heat treatments. With a maximum soluble copper content of 5.7% [28], the copper alloying elements can occur within the matrix or as intermetallic particles [29]. Due to the solubility nature of copper in aluminum, with appreciably higher solubility at higher temperatures in comparison to lower temperatures, one can expect precipitation of an Al-Cu secondary phase during solidification.

Considering the binary phase diagram shown in Figure 1-12, the maximum solute solubility of copper in aluminum is 5.7 wt.%, occurring at the eutectic melting point temperature of 548°C. This aluminum phase region is designated as α and is representative aluminum's face-centered cubic (*fcc*) microsctructure.

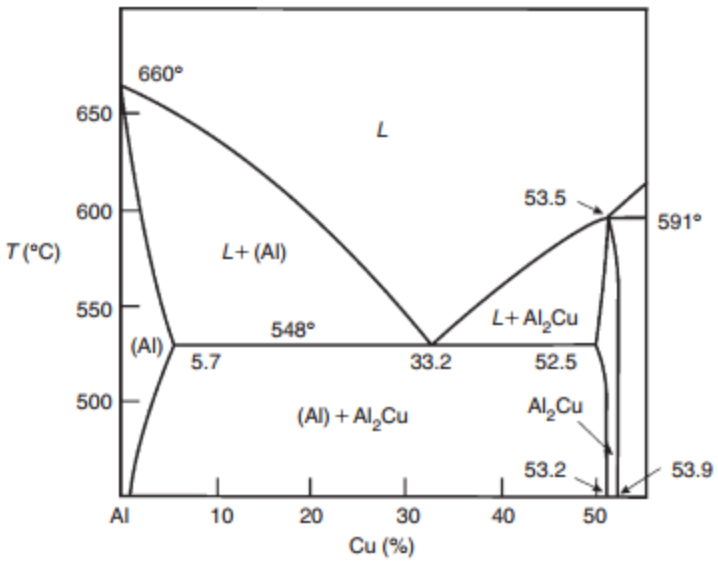

Figure 1-12 Al-Cu Binary Phase Diagram [28]

During initial solidification, the fine precipitates are formed in the shape of disk-shaped clusters called Guinier Preston (GP) Zones. These GP zones are rich in the solute and are inherently coherent with the aluminum matrix. With increasing temperature and/or increasing time, these precipitates undergo growth and gradually become less coherent with the aluminum matrix. This can be described by the following sequence of events, where the supersaturated solid solution (*SSS*) transitions to the GP zone region and into the θ-phase (Al_2Cu) precipitates.

$$SSS \rightarrow GP \rightarrow \theta'' \rightarrow \theta' \rightarrow \theta$$

It is within the θ'' and θ' metastable regions where one can attain the highest strength conditions [30]. These regions maintain their coherency within the matrix and have an identical tetragonal structure to the GP zones but are different in terms of the precipitate thickness. With continued precipitate growth, the precipitate begins to tend towards the equilibrium θ, resulting in a softer alloy. It is at this stage when the alloy is deemed to be overaged.

Al-Cu-Mg Ternary Phase System and the Effects of Minor Alloying Elements

Like the Al-Cu binary system, the Al-Cu-Mg ternary system undergoes similar precipitation growth stages. With regards to AA2024, we will be expecting a mixture of the α, θ and *S* phases,

as seen in Figure 1-13. These secondary phases are typically categorized as constituent particles, dispersoids and precipitates.

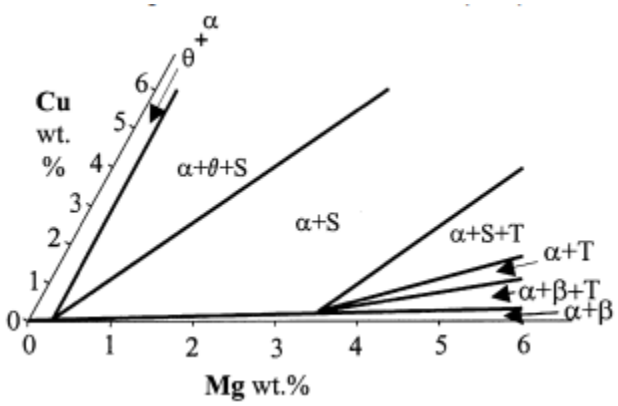

Figure 1-13 Distribution of solid state phases in the Al-Cu-Mg system at 200 °C [31]

Constituent particles are formed by a reaction in the liquid-solid eutectic region during solidification and can range from one to tens of μm in size. The particle sizes shrink with increasing solidification rate and with increasing deformation caused by mechanical processes such as hot rolling. The constituent phases, however, become less soluble with increasing Fe and Si content, due to their inherent solubility in aluminum. If insoluble, the presence of constituent particles may become a source of crack growth and corrosion while offering no improvement to mechanical properties. This is especially apparent when considering the relationship between fracture toughness and Fe/Si content, as shown in Figure 1-14 [32]. Due to the nature of the HSBC process and its moderately high solidification rate, it is expected the constituent particles will be smaller in comparison to DC cast products.

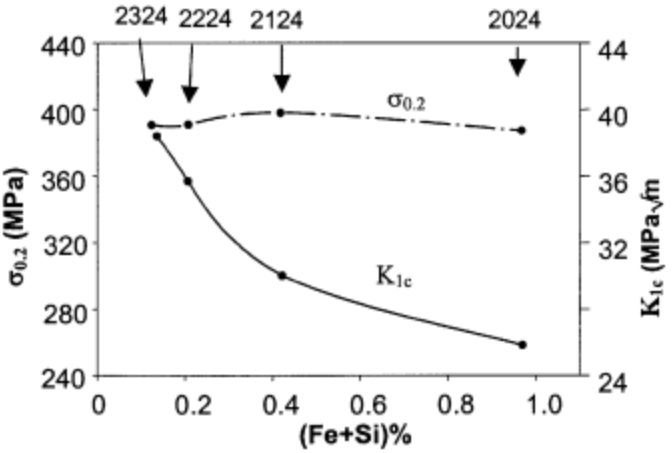

Figure 1-14 Effect of Fe and Si content on strength and fracture toughness in 2X24 aluminum alloys [32]

Dispersoids are created during long term heat treatments in a solid-solid reaction and used as resistors towards recrystallization. The size lies in the range of 10-200 nm and in the case of AA2024, are in the form $Al_{20}Cu_2Mn_3$, as shown in Figure 1-15 [33]. Dispersoids, *T* phase in Figure 1-13, are made up of low solubility elements like Mn and thus are difficult to dissolve during thermal heat treatments.

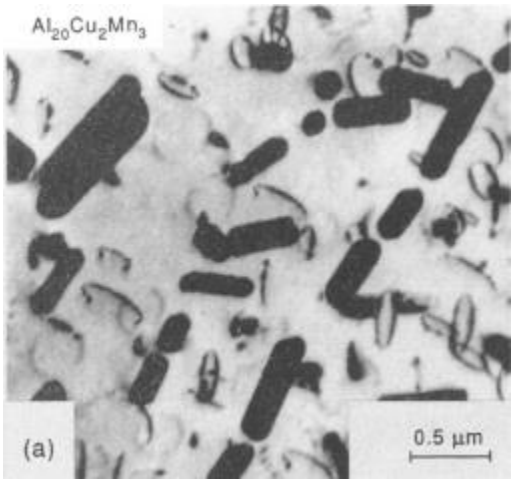

Figure 1-15 TEM images showing dispersoids in AA2024 alloy [33]

Precipitates found in Al-Cu-Mg based alloys are like those found in Al-Cu based alloys. Bagaryatsky proposed a novel precipitation sequence for the Al-Cu-Mg system [34]. The Guinier-Preston-Bagaryatsky (GPB) zone replaces the previous GP zones, while the *S* region ($CuMgAl_2$) substitutes the θ (Al_2Cu) region found in Al-Cu alloys. The precipitation growth sequence proposed by Bagaryatsky is as follows:

$$SSS \rightarrow GPB \rightarrow S" \rightarrow S' \rightarrow S$$

Over the 60 years since the proposed GPB zones and the accompanied growth sequence, numerous studies have been performed to confirm the sequence and the subsequent regions. It has been determined that since S' and *S* have identical structures but only differ in terms of the lattice parameters. Due to this, it is deemed that they have no distinction between each other [34]. Similarly, the distinction between GPB regions and S'' has been researched thoroughly to no conclusive avail [35, 36]. This has caused some to continue naming the region as a GPB zone, while others have adopted the term Mg/Cu clusters (or co-clusters). Due to the lack of concrete evidence of the existence of a GPB region and more recent evidence of Mg/Cu clusters, S.C. Wang *et al.* proposed the following growth sequence [34]:

$$SSS \rightarrow Mg/Cu\ Clusters \rightarrow S" \rightarrow S$$

Precipitates can greatly affect the strength of the material via precipitation strengthening in combination with aging, as shown in Figure 1-16. It is important to note the relatively higher hardness increase in the AA2618 alloy. Alloys with a lower Cu:Mg ratio (~0.5-2) lie in the α + *S* region (Figure 1-13) exhibit a more significant two step hardening sequence in comparison to alloys in the α + θ + *S* region [37]. For alloys with a medium Cu:Mg ratio (2-4), although they lie in the α + θ + *S* region, the primary precipitation phase remains to be the *S* phase, thus leading to the similar two step hardening sequence [38, 39].

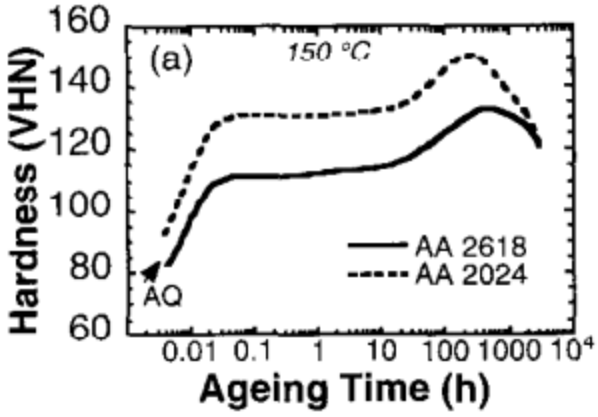

Figure 1-16 Hardness and aging time at 150 C for AA2024 and AA2618 alloys [40]

The widely accepted mechanism explaining the initial increase in hardness, first proposed by Ringer *et al.*, is the tendency to produce coherent Mg/Cu clusters [40]. Liu *et al.* looked further into the age hardening mechanism, specifically aging at 170 °C and came to several conclusions [41]. First, the total critical shear stress of the Mg/Cu clusters remain predominantly constant at the hardness plateau despite the changing number density and volume fraction of Mg/Cu clusters during ageing. Second, the shear modulus of the Mg/Cu clusters were found to be independent of aging time (at 170°C). Third, the second stage of age-hardening is primarily caused by the significant order hardening effect.

Ultimately, understanding the three hardening mechanisms proposed (chemical, modulus and order hardening) is of great importance in further understanding the strengthening of the Al-Cu-Mg alloys. Order hardening is caused by short or long range ordered phase interacting with the dislocations. In the case of Al-Cu-Mg alloys, the ordered phase is of extremely short range [42]. Modulus hardening is caused by the difference in shear modulus between the clusters and the matrix. Chemical hardening is caused by the interfacial energy between the precipitates and the matrix. As the interfacial energy is linearly related to the chemical hardening and given that both are of significantly smaller magnitude to both the modulus hardening and order hardening, it can be deemed negligible [42].

Casting of AA2024

The biggest concern with casting aluminum alloys is the effect of the alloying elements to the fluidity, porosity, hot tearing and segregation of alloying elements. Understanding the castability of an aluminum alloy will allow one to optimize the product quality and minimize casting defects.

It has been estimated that DC casting accounts for approximately 25 MT per year of aluminum production globally [43]. Eskin summarizes the DC casting process in Reference [44]. Traditionally, AA2024 has been cast by DC casting in the form of large cross-sectional slabs. Several common issues are present in the casting of AA2024 via the DC casting process that must be addressed. First is the segregation of the alloying elements, primarily copper and magnesium, within the billet. Q. Du *et al.* showed the segregation profiles of both copper and magnesium (Figure 1-17) and showed a very similar segregation profile between both alloying elements [45]. In a similar manner, Aboutalebi analyzed the effects of Electromagnetic Stirring (EMS) on the effects of copper and magnesium segregation in AA2024 [46]. To minimize segregation of alloying elements, EMS is often employed to induce stirring, reduce SDAS and ultimately have a more uniform distribution of elements.

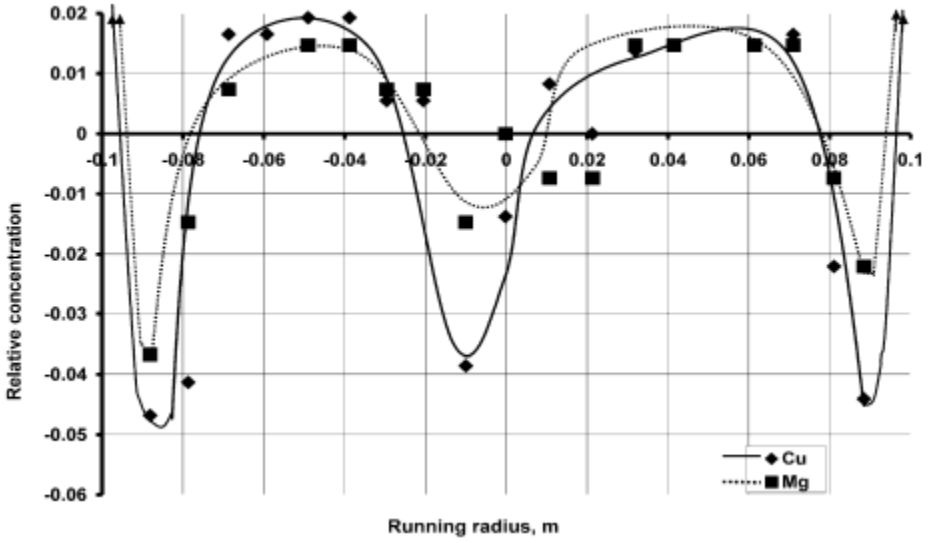

Figure 1-17 Experimentally observed macrosgreation of Cu and Mg in a 200-mm round billet cast of grain refined AA2024 cast at 12 cm/min [45]

Due to the slower cooling rates in DC casting processes in comparison to HSBC processes, as summarized by Eskin [44] and Guthrie and Isac respectively [7], one can expect larger SDAS in DC cast products. Microstructure and grain refinement, as shown by Eskin [47], is also dictated by the superheat temperature during casting. This is shown in Figure 1-18.

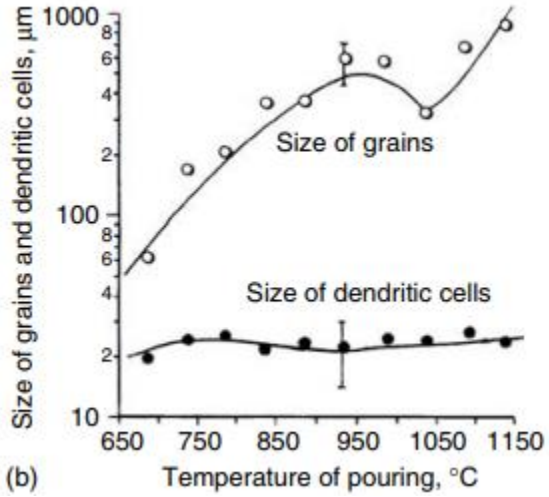

Figure 1-18 Grain and dendritic cell size over various superheats for DCC of AA2024 [47]

With regards to AA2024, casting defects is the primary concern during DC casting processes. It is well known that the alloy has a tendency for hot cracking during casting, solidification and rolling, with the primary causes being the large freezing range (136 K), high coefficient of thermal expansion, high solidification shrinkage and the segregation of alloying elements to the grain boundaries [48-51]. Paramtmuni *et al*. showed that the cracking resistance is dependent on solidification rates and can be improved by finer grain sizes and lesser amounts of generated eutectics [52]. This is one of the primary motivations to investigate the casting of AA2024 using the HSBC process.

1.4 Numerical Methods used in Metal Castings

Numerical methods are the means by which the solutions to differential equations are solved via numerical approximations. In the case of metal castings, transport phenomena problems are often found in the form of partial differential equations in which an analytical solution is often difficult or even impossible to determine. This results in numerical methods as the only method to solve

the problem in an accurate manner while also providing information that cannot be determined experimentally. In the present research, both CFD and IHCP techniques were utilized, with the following review analyzing appropriate techniques in metal castings.

1.4.1 Computational Fluid Dynamics and the HSBC process

The primary problem to be solved in the world of fluid dynamics is the Navier-Stokes equations, as expressed in conservative form in equation (2). The equations are nonlinear in nature due to the convective terms and thus are inherently difficult or impossible to solve analytically.

$$\frac{\partial(\rho u_j)}{\partial t} + \frac{\partial(\rho u_j u_i)}{\partial x_i} = -\frac{\partial P}{\partial x_j} + \mu \frac{\partial^2 u_j}{\partial x_i^2} + body\ forces \tag{2}$$

The general differential equation, as expressed by Patankar [53], is shown in equation (3), with φ representing the general variable and Γ representing the diffusion coefficient.

$$\frac{\partial}{\partial t}(\rho\phi) + \frac{\partial}{\partial x_j}\left(\rho u_j \phi\right) = \frac{\partial}{\partial x_j}\left(\Gamma \frac{\partial}{\partial x_j}\phi\right) + S \tag{3}$$

To solve the general differential equation, equation (2), often used for energy, mass transfer or turbulent quantities or the Navier-Stokes equation, equation (1), control volume finite difference methods can be used to discretize the equations. A two-dimensional discretization scheme, as shown in Figure 1-19, is used to produce algebraic expressions from differential expressions, with them being solved with combinations and variations of Gauss-Seidel and diagonal (tri-diagonal, penta-diagonal) matrix algorithms.

With the following techniques in mind, the next step is the pressure-velocity coupling to handle the pressure and velocity field within the solution domain. In the case of metal castings, the SIMPLE, SIMPLER and the PISO schemes are popular choices in research.

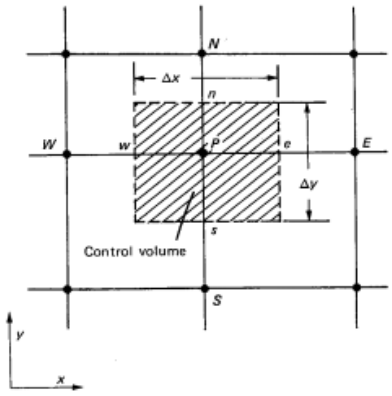

Figure 1-19 Control volume for a two-dimensional cartesian coordinate system [53]

Patankar, to improve the rate of converge, revised the SIMPLE scheme and the results became the SIMPLER scheme, or SIMPLE revised [54]. Due to the exaggerated pressure corrections arising in the SIMPLE scheme, the need for underrelaxation was necessary to improve convergence rates. Additionally, the lack of information from neighboring nodes proved to be inefficient in the correction of the pressure field. As a result, a scheme in which the pressure-correction equation is solely used to correct velocities while the pressure field is solved using equation (5) and (6). In other words, the SIMPLER scheme does not guess pressure fields but rather deduces them from a given velocity field.

$$a_P P_P = \sum a_{nb} P_{nb} + b \tag{5}$$

$$b = \frac{(\rho_P^0 - \rho_P)\Delta x \Delta y \Delta z}{\Delta t} + [(\rho \hat{u})_w - (\rho \hat{u})_e]\Delta y \Delta z + [(\rho \hat{v})_s - (\rho \hat{v})_n]\Delta z \Delta x + [(\rho \hat{w})_b - (\rho \hat{w})_t]\Delta x \Delta y \tag{6}$$

The PISO scheme was first proposed by Issa [55, 56] in 1986 as an alternative to the SIMPLE and SIMPLEC schemes. By describing the pressure and velocity as dependent variables, Issa showed that one can split the solution process into a series of steps, resulting in decoupling of pressure and velocity. Furthermore, the solution eliminates iterations by using a predictor step and two corrector steps, allowing for quicker computing times and more stable results. As a result, it is often applied in transient problems where there is either weak or no coupling between the momentum and scalar equations.

The nature of metal castings, however, are often turbulent in nature, thus requiring the use of turbulent models and turbulence quantities. The Reynolds Averaged Navier Stokes (RANS) equations are used to evaluate turbulent flows. The equations are produced by Reynolds decomposition, where the instantaneous quantities are decomposed into time-averaged and fluctuating components. By doing so, one can present the incompressible continuity equation and the RANS equation in equation (7) and (8) respectively:

$$\nabla \cdot u_i = 0 \tag{7}$$

$$\frac{\partial \bar{u}_i}{\partial t} + \frac{\partial (\bar{u}_i \bar{u}_j)}{\partial x_j} = \frac{\partial}{\partial x_j}\left[\nu\left(\frac{\partial \bar{u}_i}{\partial x_j}\right) - \overline{u_j' u_i'}\right] - \frac{1}{\rho}\frac{\partial \bar{p}}{\partial x_i} + \mathrm{S} \tag{8}$$

To provide closure to the following equation and solve the viscous stresses ($\overline{u_j' u_i'}$), one uses different turbulence models. An understanding of several popular turbulent models is important as they are applied for different applications. The most popular is the well known k-ε model, first conceived by Launder and Spalding in 1973 [57]. The transport terms in the model, turbulence kinetic energy (k) and the rate of dissipation of turbulence energy (ε) is solved by the following two transport equations, where $\frac{D}{Dt} = \frac{\partial}{\partial t} + u_i \frac{\partial}{\partial x_i}$ represents the convective time derivative:

$$\frac{D\epsilon}{Dt} = \frac{1}{\rho}\frac{\partial}{\partial x_j}\left[\frac{\mu_t}{\sigma_\epsilon}\frac{\partial \epsilon}{\partial x_j}\right] + \frac{C_1 \mu_t}{\rho}\frac{\epsilon}{k}\left(\frac{\partial U_i}{\partial x_j} + \frac{\partial U_j}{\partial x_i}\right)\frac{\partial U_i}{\partial x_j} - C_2 \frac{\epsilon^2}{k} \tag{9}$$

$$\frac{Dk}{Dt} = \frac{1}{\rho}\frac{\partial}{\partial x_j}\left[\frac{\mu_t}{\sigma_k}\frac{\partial k}{\partial x_j}\right] + \frac{\mu_t}{\rho}\left(\frac{\partial U_i}{\partial x_j} + \frac{\partial U_j}{\partial x_i}\right)\frac{\partial U_i}{\partial x_j} - \epsilon \tag{10}$$

The turbulent viscosity is expressed as:

$$\mu_t = C_\mu \, \rho k^2 / \epsilon \tag{11}$$

The constants within the two transport equations have been determined through extensive work by Launder *et al*. for the case of free turbulent flow and are given in Table 1-2 [58]

Table 1-2 Constants for the k-ε model, as determined by Launder et. al [58]

C_μ	C_1	C_2	σ_k	σ_ϵ
0.09	1.44	1.92	1.0	1.3

This model has given good results for various metal castings. Guthrie and Tavares used the METFLO code and a low-Reynolds k-ε turbulent model to evaluate the transport phenomena of steel using twin-roll casting (TRC) and horizontal single belt casting (HSBC) processes [59]. Jefferies used a similar model to evaluate the HSBC production of thin strip steel and validated it against water models [60]. The k-ε showed reliance on appropriate near wall approximations, due to the laminar nature of the fluid flow near the wall. Thus arises the use of k-ω turbulence models.

Wilcox developed the k-ω turbulence model as an alternative two-equation model to the k-ε model that allowed for better solution in the near wall regime, as compared to the free stream [61]. The two equations of the model showing the transport of turbulence kinetic energy, k, and the specific rate of turbulence dissipation, ω, are shown equation (12) and (13) respectively. The adoption of the k-ω model was appropriate in the case of the HSBC process. Ge *et al*. utilized the k-ω model to evaluate fluid flow, heat transfer and solidification of the HSBC process [13]. The Nikuradse equivalent sand-grain roughness model was used to model the surface roughness and to model solidification initiation. Furthermore, Ge *et al.* showed that the model allowed for an accurate representation of both the meniscus behavior and the interfacial heat transfer, as shown in Figure 1-20.

$$\frac{Dk}{Dt} = \tau_{ij}\frac{\partial u_i}{\partial x_j} - \beta^* k\omega + \frac{\partial}{\partial x_j}\left((\nu + \sigma^*\nu_T)\frac{\partial k}{\partial x_j}\right) \tag{12}$$

$$\frac{D\omega}{Dt} = \alpha\frac{\omega}{k}\,\tau_{ij}\frac{\partial u_i}{\partial x_j} - \beta\omega^2 + \frac{\partial}{\partial x_j}\left((\nu + \sigma\nu_T)\frac{\partial \omega}{\partial x_j}\right) \tag{13}$$

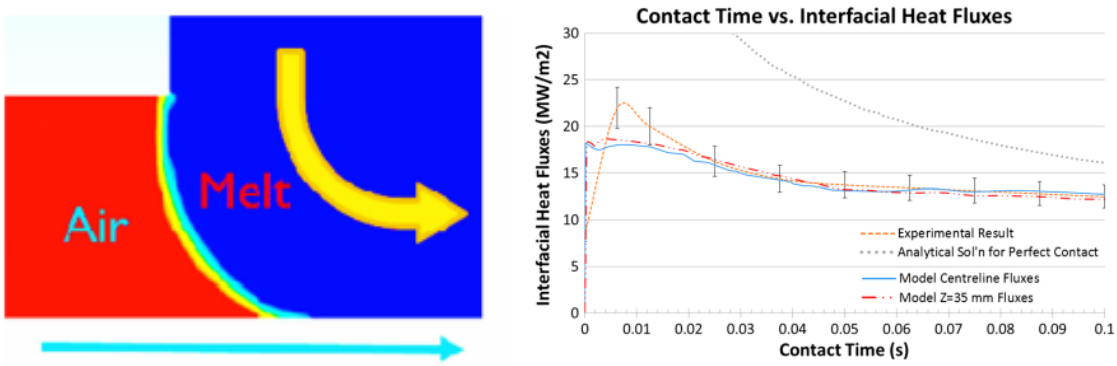

Figure 1-20 Meniscus behavior at the triple point (Left) and the Interfacial heat transfer behavior comparison between numerical and experimental results (Right) [13]

Due to the k-ω model's poor ability to evaluate the free stream behavior, the shear stress transport (SST) k-ω model, as developed by Menter [62], is believed to be a more valuable approach to tackling metal casting problems. The primary model uses a k-ω model within the boundary layer through the viscous sub-layer and all the way to the wall, making it appropriate as a low-Re turbulence model. The k-ε is then used within the free stream regime. The two transport equations for the turbulence kinetic energy and specific dissipation rates are shown in equations (14) and (15) respectively, while the eddy viscosity is shown in equation (16). F_2 is a function that is one for boundary-layer flows and zero for the free shear flow while α_1 is a constant.

$$\frac{Dk}{Dt} = \frac{\partial}{\partial x_j}\left((\nu + \sigma_k \nu_T)\frac{\partial k}{\partial x_j}\right) + P_k - \beta^* k\omega \tag{14}$$

$$\frac{D\omega}{Dt} = \frac{\gamma P_k}{\rho \nu_t} - \beta\omega^2 + \frac{\partial}{\partial x_j}\left[(\nu + \sigma_\omega \nu_T)\frac{\partial \omega}{\partial x_j}\right] + 2(1 - F_1)\sigma_{\omega 2}\frac{1}{\omega}\frac{\partial k}{\partial x_j}\frac{\partial \omega}{\partial x_j} \tag{15}$$

$$\nu_T = \frac{\alpha_1 k}{\max(\alpha_1 \omega, SF_2)} \tag{16}$$

Jonayet and Thomas [63], Kratzsch *et al.* [64], and Timmel and Miao [65-67] used the k-ω SST model to determine the fluid behavior in steel continuous casting molds. Pelss *et al.* used the same turbulent model to look at twin roll casting of stainless steel [68]. Ge *et al.* similarly applied the turbulent model to the HSBC process, evaluating the multiphase flow and solidification of low carbon steels [17].

1.4.2 IHCP Methods in Metal Castings

IHCP, also known as Inverse Heat Transfer Problems (IHTP), methods are numerical methods used to solve unknown boundary conditions or fluid properties. Problems are deemed direct when the boundary condition to a problem, whether they be surface heat flux or temperature histories, are known and well defined. The problem is further considered as well-posed if it meets the following requirements:

1. The solution must exist
2. The solution must be unique
3. The solution must be stable with respect to perturbation on the input and the solution must depend continuously on the input (the boundary condition)

In the case of IHCP, the boundary conditions are not known and must be deduced by measurements in the interior of the problem domain. In this case, the problem is considered "ill-posed" due to its failure to satisfy requirement 3, as the solution does not depend continuously to the input. In addition, the result of small perturbations, caused by measurement errors or electrical fluctuations, can have a significant impact on the solution.

In the case of metal castings, there are two primary problems that need to be tackled. The first is a boundary value determination problem. In this case, temperature measurements are taken inside internal points and the surface temperature or heat flux is determined via IHCP methods. The problem derivation is shown in equations (17-19), assuming a heat source Q at a known location x_s, as shown in Figure 1-21.

$$\frac{\partial}{\partial x_j}\left(k\frac{\partial T}{\partial x_j}\right) + Q = \rho C\frac{\partial T}{\partial t} \tag{17}$$

$$Q(r,t) = g_p(t)\delta(x - x_s) \tag{18}$$

$$\delta(r) = \begin{cases} \infty & x = 0 \\ 0 & else \end{cases} \tag{19}$$

The total inverse problem is described in equation (20), with initial conditions and boundary conditions shown in equations (21) and (22) respectively, assuming a domain Ω with boundary δΩ.

$$\rho C \frac{\partial T(x,t)}{\partial t} = \frac{\partial}{\partial x_j}\left(\frac{k \partial T}{\partial x_j}\right) + g_p(t)\delta(x - x_s), \quad (x,t) \in \Omega \times (0, t_f) \tag{20}$$

$$\frac{\partial T(x,t)}{\partial t} = 0, \quad (x,t) \in \delta\Omega \times (0, t_f) \tag{21}$$

$$\frac{\partial T(boundaries,t)}{\partial x_j} = 0 \tag{22}$$

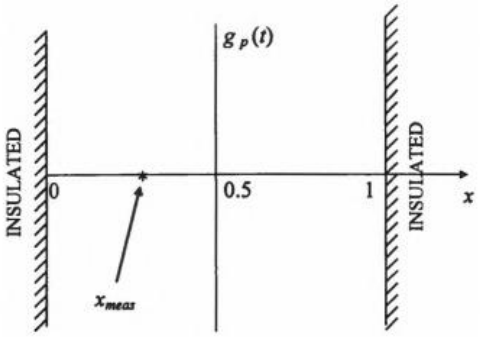

Figure 1-21 Physical geometry of the IHCP problem, assuming a heat source at x = 0.5 [69]

The solution method for an IHCP is one that must be stable with respect to measurement errors and time step size, have statistical bias and have reasonable computing cost and implementation. This lead to the widely adopted least squares method (i.e. the sum of squared residuals) for the solution of IHCP problems [70, 71]. This is shown in equation (23), where *S* is the objective function (or cost function), *Y* and *T* are vectors containing the measured and direct solution temperatures respectively and the superscript *T* indicating the transpose of the vector with all being taken at times *i* = 1, 2,… I:

$$S = (Y - T)^T (Y - T) = \sum_{i=1}^{I} (Y_i - T_i)^2 \tag{23}$$

In the case where the standard deviation is fluctuating, a diagonal weighting matrix W is applied to the objective function, where σ is the standard deviation of the measurement, to yield:

$$S_W = (Y - T)^T \, W(Y - T) = \sum_{i=1}^{I} \frac{(Y_i - T_i)^2}{\sigma_i^2} \tag{24}$$

When the number of unknown parameters is large, such as in the case of an unknown transient boundary condition, the solution may oscillate and become unstable. The application of Tikhonov's regularization is a common method to reduce the solution's oscillating behavior [72, 73]. The first-order regularization procedure for a lone sensor requires the minimization of the following function:

$$S[f(t)] = \sum_{i=1}^{I} (Y_i - T_i)^2 + \alpha \sum_{i=1}^{I-1} (f_{i+1} - f_i)^2 \tag{25}$$

Note, the importance in the selection of the α term is thoroughly discussed by Tikhonov [74, 75], Beck [76], Morozov[77, 78] and Zabaras [79]. It has been concluded that the selection of the α term should be chosen such that the measurement error is consistent with that of the estimation error of the flux q. The issue arises when the error is unknown, which is the likely case. In this situation, the α term tends to be chosen such that the solution becomes smooth during the minimizing of the objective function S.

Once the regularization methods are applied, the Levenberg-Marquadt Method or the Conjugate Gradient Method are the most commonly used parameter estimation techniques, especially in the case of metal castings. The Levenberg-Marquadt Method is an iterative method first conceived by Levenberg in 1944 for the solution of non-linear problems using a least squares method [80], before Marquadt, in 1963, derived a similar technique also using a least-squares method [70]. By parameterizing the source, in this case the boundary heat flux, one can simplify it with an unknown parameter P and known trial functions (i.e. polynomials, B-Splines, etc.) C. This is shown in equation (26), where N indicates the number of unknown parameters.

$$q(t) = \sum_{j=1}^{N} P_j C_j(t) \tag{26}$$

Assuming an ordinary least squares regularization, the basic procedure is as follows:

1. Solve the direct problem using the current estimated time dependent heat flux *q(t)* to get the transient temperature field. Obtain a temperature vector over time for the position at which the temperature sensor is located.
2. Compute the objective function as shown in equation (25), where P^k is the vector of unknown parameters, as parameterized by equation (26).

$$S(P^k) = [Y - T(P^k)]^T [Y - T(P^k)] \tag{27}$$

3. Compute the sensitivity matrix J^k and then the matrix Ω^k using equations (28) and (29) respectively using the current known parameters.

$$J(P) = \left[\frac{\partial T^T(P)}{\partial P}\right]^T \tag{28}$$

$$\Omega^k = diag[(J^k)^T J^k] \tag{29}$$

4. Solve the linear system of algebraic equations using the Levenberg-Marquadt Method using equation (30)

$$\Delta P^k[(J^k)^T J^k + \mu^k \Omega^k] \quad = (P^{k+1} - P^k)[(J^k)^T J^k + \mu^k \Omega^k] \quad = (J^k)^T [Y - T(P^k)] \tag{30}$$

5. Compute the new estimate $P^{k+1} = P^k + \Delta P^k$
6. Return to step 1 and solve the direct problem with the newly estimated P^{k+1}
7. If $S(P^{k+1}) \geq S(P^k)$ replace μ^k by $10\mu^k$ and return to step 4
8. If $S(P^{k+1}) < S(P^k)$, use the new P^k value and replace μ^k by 0.1 μ^k
9. If one of the following criterion (equation 31-33) is satisfied, end the program; otherwise, return to step 3.

$$S(P^{k+1}) < \epsilon_1 \tag{31}$$

$$|(J^k)^T [Y - T(P^k)]| < \epsilon_2 \tag{32}$$

$$|P^{k+1} - P^k| < \epsilon_3 \tag{33}$$

The Conjugate Gradient Method (CGM) proceeds in a very similar manner to that of the Levenberg-Marquadt Method, with the major difference being the iterative procedure. During each iteration, the direction of descent is determined using a linear combination of negative gradient direction at the current iteration compared to the previous one. Then an appropriate step size is taken along the direction of descent to minimize the objective function. The complete process is described as follows:

1. Solve the direct problem using the current estimated time dependent heat flux *q(t)* to get the transient temperature field. Obtain a temperature vector over time for the position at which the temperature sensor is located.
2. Check if the stopping criterion, as shown in equation (33), is satisfied. If not, proceed to step 3
3. Compute the sensitivity matrix using equation (28)
4. Calculate the gradient direction $\nabla S(P^k)$ by using equation (34). Then calculate the conjugation coefficient γ^k using the Polak-Ribiere expression [81] (equation (35)) or the Fletcher-Reeves expression [82] (equation (36))

$$\nabla S(P^k) = -2(J^k)^T[Y - T(P^k)] \tag{34}$$

$$\gamma^k = \frac{\sum_{j=1}^{N}\left\{[\nabla S(P^k)]_j[\nabla S(P^k) - \nabla S(P^{k-1})]_j\right\}}{\sum_{j=1}^{N}[\nabla S(P^{k-1})]_j^2} \tag{35}$$

$$\gamma^k = \frac{\sum_{j=1}^{N}[\nabla S(P^k)]_j^2}{\sum_{j=1}^{N}[\nabla S(P^{k-1})]_j^2} \tag{36}$$

5. Calculate the direction of descent using equation (37)

$$d^k = \nabla S(P^k) + \gamma^k d^{k-1} \tag{37}$$

6. Compute the search step size using equation (38)

$$\beta^k = \frac{[J^k d^k]^T[T(P^k) - Y]}{[J^k d^k]^T[J^k d^k]} \tag{38}$$

7. Compute the new estimate P^{k+1} using equation (39) and return to step 1.

$$P^{k+1} = P^k - \beta^k d^k \tag{39}$$

Both the Levenberg-Marquadt Method and Conjugate Gradient Method are commonly found in metal casting applications [83-85], offering both ease of computational coding, speed and accuracy. Martorano and Capocchi [86] used IHCP methods and experimental methods to determine the heat transfer coefficient at the metal-mould interface. A least squares method was used alongside six R type thermocouples to determine the heat transfer coefficient and the temperature field, with the direct solution solved using a finite volume method with 16 nodes. Figure 1-22 shows the solution between the transient temperature field solved by IHCP and that of the measured temperatures are well matched.

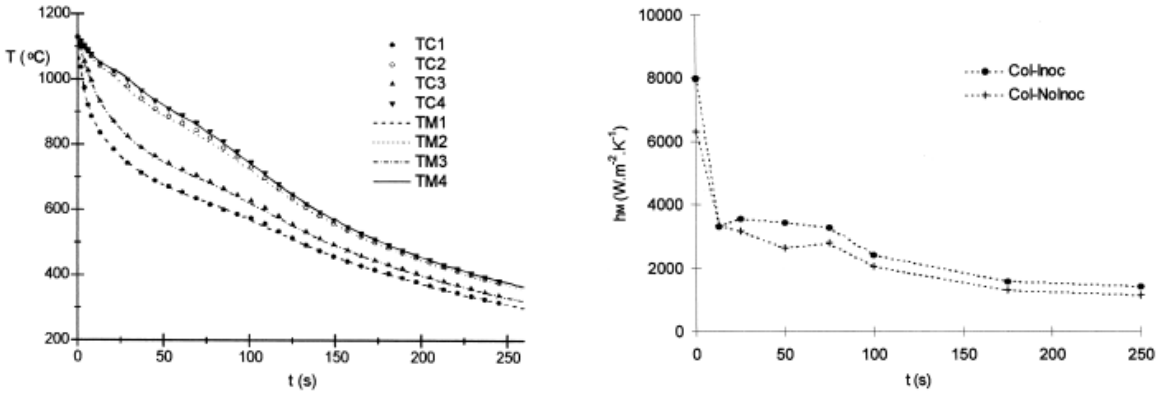

Figure 1-22 Transient temperature fields solved by IHCP compared to measured temperatures (Left) and the solved heat transfer coefficients for two different parameters (Right) [86]

Another IHCP approach was developed by Tavares in its application for vertical twin-roll casters using an explicit heat transfer model [87]. Using an adjusted objective function with a second order regularization function, as shown in equation (40), heat fluxes are guessed and evaluated to minimize this objective function. This was compared to function specification methods and space marching techniques, with the results showing a second order regularization method resulted in the most accurate results.

$$S[f(t)] = \sum_{i=1}^{I}(Y_i - T_i)^2 + \alpha \sum_{i=1}^{I-1}(f_{i+1} - 2f_i + f_{i-1})^2 \tag{40}$$

1.5 Literature Summary and Research Motivation

In the present literature review, it has been shown that the HSBC process is an appropriate casting alternative to produce AA2024 strips. An understanding of the heat transfer and fluid flow will dictate the success of the HSBC process. As summarized, CFD and IHCP techniques will be appropriate to evaluate the transport phenomena within the process. From the literature review, the following conclusions can be made:

1. The HSBC process is a cost and energy efficient alternative to produce near net shape products. The viability of the process will depend on the macro and micro properties of the strip product.
2. AA2024 casting defects are dependent primarily on the interfacial heat transfer and solidification rate of the liquid melt. By using the HSBC process, it is expected that the risk of casting defects will be minimal
3. To evaluate the fluid flow, CFD analysis will be appropriate to study surface and meniscus behavior of the liquid melt. Furthermore, delivery system evaluation can be performed using CFD analysis. A k-ω SST model with a PISO velocity pressure coupling technique will be the most appropriate solution technique to solve the fluid flow.
4. Interfacial heat transfer can be determined both by CFD analysis and validated using IHCP techniques. Second order regularization methods applied to minimizing the objective function will be the most appropriate solution technique to solving the interfacial heat flux.

1.6 Objectives and Outline of this Thesis

The objectives of the present study will include three stages. First, a numerical analysis will be performed to predict and evaluate the fluid flow behavior of AA2024 using the HSBC process. A transient, turbulent fluid flow model will be used to evaluate the fluid flow. The information determined will allow for the second stage: a successful simulator and pilot-scale cast of AA2024 using the HSBC process. Casting preparations, alloying and casting will be performed at the Stinson Laboratories. The following strip products will be evaluated in the third stage. Surface

quality, porosity and microstructure will be analyzed using optical microscopy and evaluated against DC cast products.

The present thesis is divided into five chapters:

Chapter 1 reviews the existing literature on the HSBC process, casting of AA2024 and numerical techniques using in metal castings.

Chapter 2 presents the development and results of the numerical analysis of casting AA2024 using the HSBC process. A transient, turbulent flow model will be used via the commercial software ANSYS Fluent to evaluate the fluid flow.

Chapter 3 describes the procedure and development of the HSBC simulator and HSBC pilot-scale caster.

Chapter 4 presents the results of the HSBC simulator and HSBC pilot-scale caster experiments. Microstructure, porosity and surface quality results will be presented in this chapter as well as mechanical properties.

Chapter 5 provides a summary of the present thesis.

Chapter 2 Numerical Analysis of the HSBC Process

In this chapter, the development and results of the CFD transient, multi-phase turbulent model are presented for the casting of AA2024 using the HSBC process. The commercial software, ANSYS Fluent, was used to prepare the simulation regime, discretize the equations, develop the models and solve.

2.1 Problem Statement – HSBC process with an inclined delivery system

The HSBC delivery system to be analyzed is shown in Figure 2-1. Liquid metal enters through the nozzle at a width of w_n before impinging on the inclined delivery system, at a height of h_r and incline angle θ. These values are summarized in Table 2-1.The liquid metal then impinges on the copper belt, at a meniscus gap height of h_m. To understand the quality of the final strip product, one must understand the fluid flow and heat transfer phenomena involved in relation to the fluid, AA2024, and the delivery system parameters. To simplify the problem several assumptions are made. First, it is assumed that the fluid behaves as a Newtonian, incompressible fluid and that the transport properties are constant. Second, a constant temperature boundary condition was used to model the water-cooled belt. Third, all other solid surfaces are modeled as adiabatic and impermeable with no slip boundary conditions. Fourth, thermal buoyancy effects were ignored. With the following assumptions, a 2-D model was developed.

Table 2-1 Numerical model parameters with respect to Figure 2-1

w_n	h_r	h_m	θ	Belt Length
2.5 mm	14 mm	0.5 mm	45°	50 mm

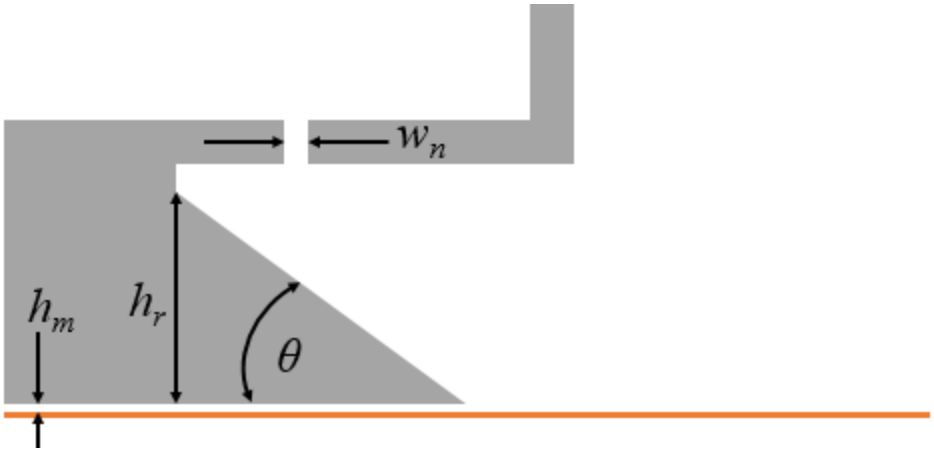

Figure 2-1 Schematic of the pilot-scale HSBC inclined delivery system

2.2 Governing equations and Turbulence Models

The transient turbulent flow is governed by the incompressible continuity and RANS equations, as shown in equations (7-8). To provide closure to the RANS equations, a k-ω SST turbulent model was chosen, with the governing equations shown in equations (14-15). The eddy viscosity is expressed in equation (16). As the region of focus is primarily the near wall regime, for both the inclined plane and the moving belt, it was decided that the k-ω SST turbulent model would be the most appropriate.

The primary advantage of the k-ω SST turbulent model is its use of the k-ω model within the boundary layer and the k-ε model in the free shear flow. As the k-ω allows direct integration to the wall, it provides a more accurate representation of the near wall regime. The problem arises in the free stream, where it is sensitive to the boundary conditions and input parameters [88]. By using the k-ε model in the free stream and a blending function in the intermediate regime, it has been shown that the k-ω SST turbulent model will provide accurate results, although the convergence times will be longer.

To evaluate the scalar quantities like temperature, the time-averaged transport equation, as shown in equation (40), was used with the temperature T and thermal diffusivity α. The appropriate auxiliary functions are needed to complete equation (15). As determined by Menter, the following auxiliary functions, equations (41-44), were deemed appropriate for the k-ω SST turbulent model

[62]. $CD_{k\omega}$ is the cross diffusion term, where *y* is the distance to the next surface. The constants found in the governing equations are listed in Table 2-2.

$$\frac{\partial \bar{T}}{\partial t} + \bar{u}\frac{\partial(\bar{T})}{\partial x_j} = \frac{\partial}{\partial x_j}\left(\alpha \frac{\partial \bar{T}}{\partial x_j}\right) + S_\phi - \frac{\partial \overline{u_j' T'}}{\partial x_j} \tag{40}$$

$$\tau_{ij} = \mu_t\left(\frac{\partial u_i}{\partial x_j} + \frac{\partial u_j}{\partial x_i} - \left(\frac{2}{3}\right)\frac{\partial u_k}{\partial x_k}\delta_{ij}\right) - \frac{2}{3}\rho k \delta_{ij} \tag{41}$$

$$F_1 = \tanh(arg_1^4) \tag{42}$$

$$arg_1 = \min[\max(\left(\frac{\sqrt{k}}{0.09\,\omega y}\right); \frac{500\nu}{y^2\omega}); \frac{4\rho\sigma_{\omega 2}k}{CD_{k\omega}y^2}] \tag{43}$$

$$CD_{k\omega} = \max\left(2\rho\sigma_{\omega 2}\frac{1}{\omega}\frac{\partial k}{\partial x_j}\frac{\partial \omega}{\partial x_j}, 10^{-20}\right) \tag{44}$$

Table 2-2 Constants in the k-ω SST turbulent model

σ_{k1}	$\sigma_{\omega 1}$	β_1	α_1	β^*	κ	γ_1
0.85	0.5	0.075	0.31	0.09	0.41	0.55

To model the multi-phase flow featuring the liquid melt and atmosphere, a Volume of Fluid (VOF) multiphase model was used. An explicit Geo-Reconstruct discretization scheme was used to better predict the moving interface between the liquid melt and the atmosphere. Material properties within each control volume are determined by the volume fraction of the primary and secondary phases and is expressed as follows, where P represents a general transport property and α_n represents the volume fraction of phase *n*:

$$\mathrm{P} = \alpha_2 \mathrm{P}_2 + (1 - \alpha_2)\mathrm{P}_1 \tag{45}$$

The general, volume fraction averaged transport property is then expressed as

$$\mathrm{P} = \sum \alpha_q \mathrm{P}_q \tag{46}$$

To further track the interfacial behavior, a continuum surface force (CSF) model was used to model the surface tension, with the resulting pressure difference being used as a source term in the momentum equation. In addition, a wall adhesion model was used to specify the contact angle between the fluid and wall. Both models, produced by Brackbill *et al.* [89], will allow for a better prediction of the multiphase interface.

2.3 Calculation Domain, Model Parameters and Material Properties

A highly structured, orthogonal mesh was built using the ANSYS Workbench package in order to discretize the mathematical model. The meshing grid is shown in Figure 2-2, with a cell size ranging from 3.1×10^{-5} m^2 to 9.9×10^{-4} m^2 and a total nodal count of 35000. Bias was given to the mesh sizes to give more information near the inclined ramp and in the regime south of the nozzle. Both were determined to be important in understanding the fluid flow structure after the nozzle and in the regime of the inclined ramp.

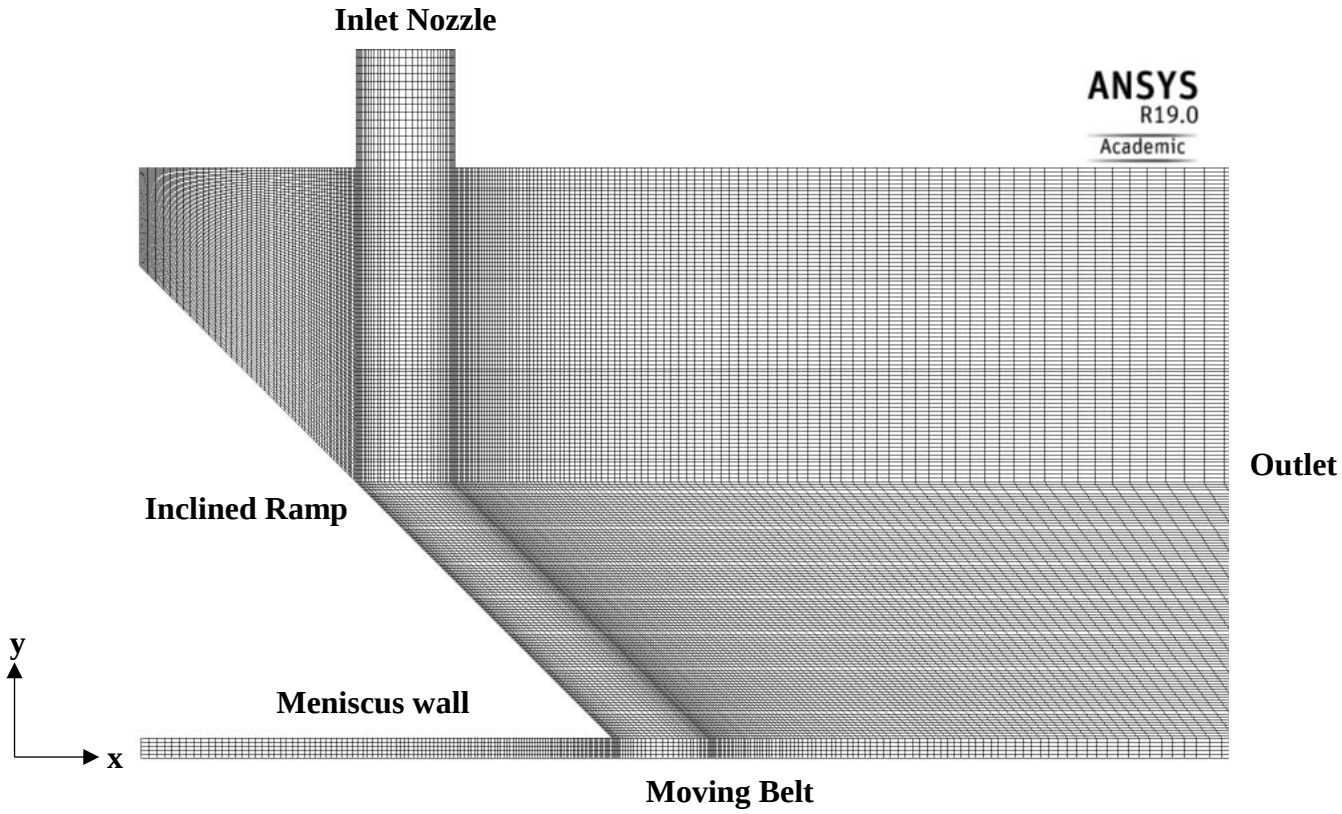

Figure 2-2 Meshing grid for the delivery system on an orthogonal coordinate system

With regards to the solution methods, a PISO scheme is used for the pressure-velocity coupling. A power law discretization scheme was used for the governing equations with a first order implicit scheme used for the transient formulation. To help convergence, under-relaxation factors were used on several properties including pressure, density, body forces, momentum and turbulent quantities. An under-relaxation factor of 0.25 was used for fluid properties while flow properties like momentum and pressure used an under-relaxation factor of 0.075. An under-relaxation factor of 0.2 was used for the turbulent quantities like k and ω.

Time steps progressed once certain convergence criterion was completed. A more severe absolute criteria of 0.0001 was used for the continuity, x-velocity and y-velocity equations as well as for the k and ω equations. An absolute criterion of 1×10^{-6} was used for the energy equation. These parameters were chosen by experience with the model and were deemed appropriate to produce accurate results. The second criteria would be a max iterations/time step of 100 to ensure progression in the model if the absolute criteria were not met.

For solid boundaries, such as the inlet walls, inclined ramp, meniscus wall and moving belt, a no slip boundary condition was used. In the case of the moving belt, a moving wall boundary condition was used with a prescribed velocity. Pressure outlets were used for the outlet conditions, with a backflow temperature of 298K and a turbulent intensity of 2%. For the inlet, a uniform velocity along the inlet length was given at a prescribed temperature. A turbulent intensity of 1% was prescribed for the inlet condition. The following conditions were determined with reference to previous CFD results of the HSBC caster by Ge *et al.* [25].

The physical properties of AA2024 and air are shown in Table 2-3. Note the surface tension coefficient and contact angle between the moving belt and liquid aluminum were previously determined by researchers at the MMPC using a high-speed camera and a plunger test.

Table 2-3 Physical Properties for AA2024 and Air

Physical Properties, Nomenclature and Units	Melt (AA2024)	Air
Density, ρ (kg/m^3)	2780	1.225
Specific heat capacity, Cp (J/kg-K)	875	1006.43
Thermal conductivity, k (W/m K)	121	0.0242
Viscosity, μ (kg/m-s)	1.22×10^{-3}	1.7894×10^{-5}
Initial Temperature (K)	940	298
Surface Tension Coefficient (N/m)	0.87	
Contact Angle along moving belt (deg)	120	
Superheat Temperature (K)	30	
Operating Belt Speed (m/s)	0.4 m/s	

2.4 Fluid flow of AA2024 using the HSBC process

The fluid flow, as shown in Figure 2-3, exhibited a similar flow behavior in comparison to the previous work by M. Xu [14-16], and is in accord with previous pilot-scale HSBC experiments. The fluid oscillates in the regime of the first impingement before reaching the belt and achieving a relatively uniform thickness. As the fluid flow impinges onto the inclined plane, a swirling flow is generated as the flow splits into two directions from the stagnation point. This is better represented in Figure 2-4 and Figure 2-5, showing the velocity profile and eddy viscosity contours respectively. The turbulence generated by the interaction with the air, the ramp and swirling flow creates an oscillating fluid structure. It is believed that this is one of the primary causes of the surface instability that later appears at the liquid melt/atmosphere interface on the moving belt. It was determined that the liquid melt height on the moving belt oscillates at an amplitude of $\pm$ 123 μm.

An understanding of the surface instability has generated interest at the MMPC, with several phenomena believed to be the root of the problem. As mentioned, the oscillation occurring at the first impingement clearly shows the oscillating liquid melt/atmosphere interface, as seen in the progression of fluid flow structure in Figure 2-3, progressing along the liquid melt.

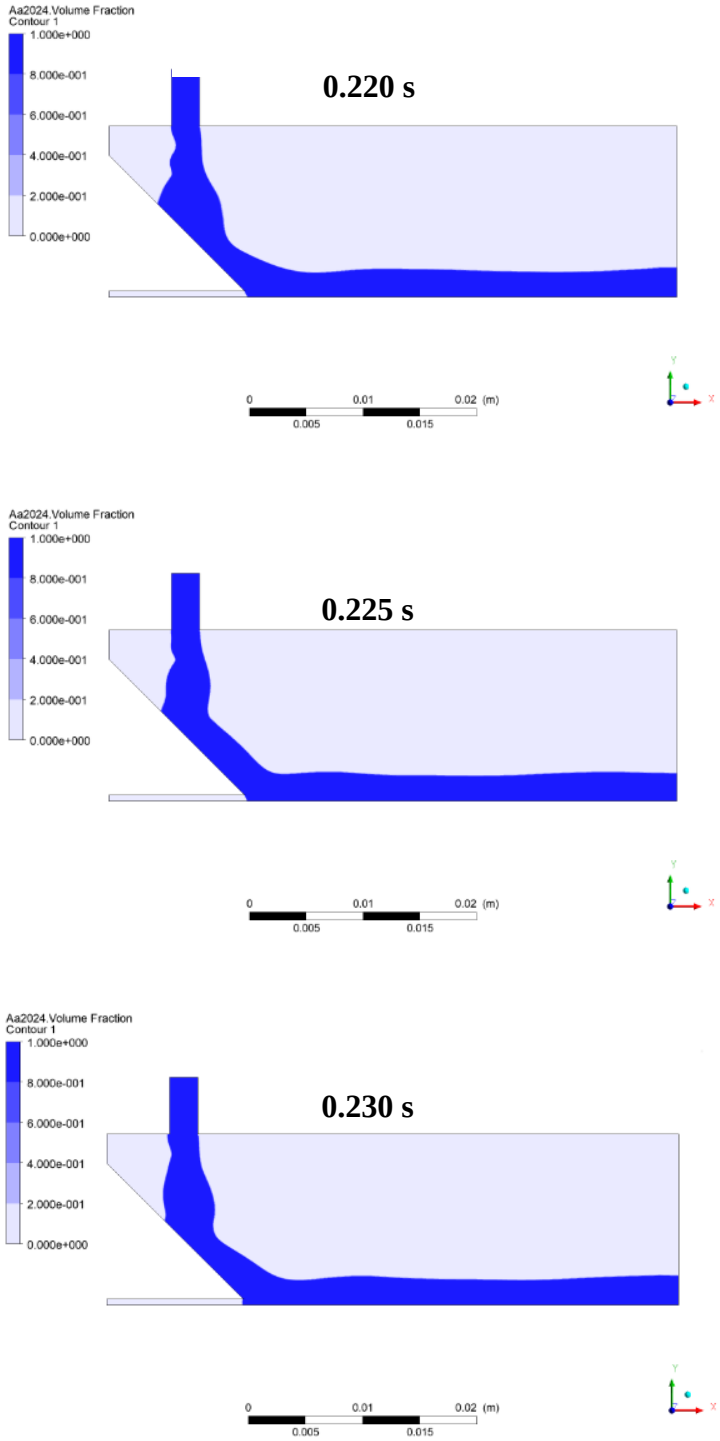

Figure 2-3 Fluid flow of AA2024 at 0.220, 0.225s and 0.230s into casting

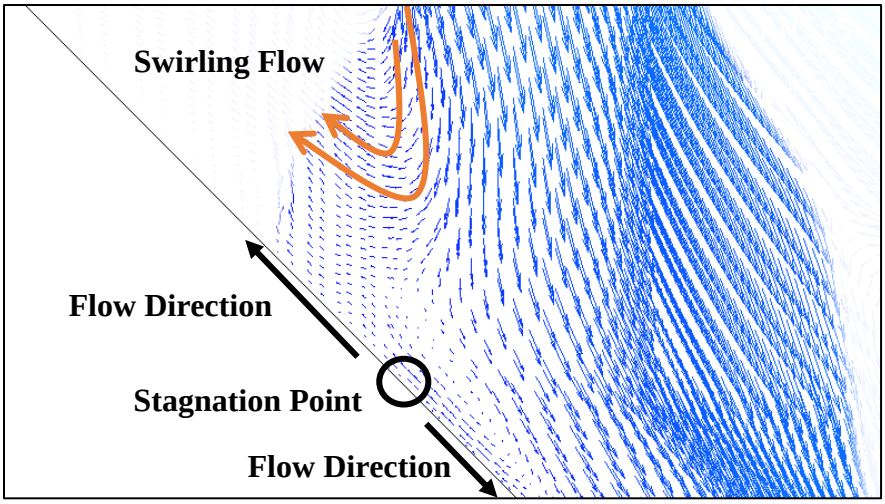

Figure 2-4 Vector velocity profile at the first impingement

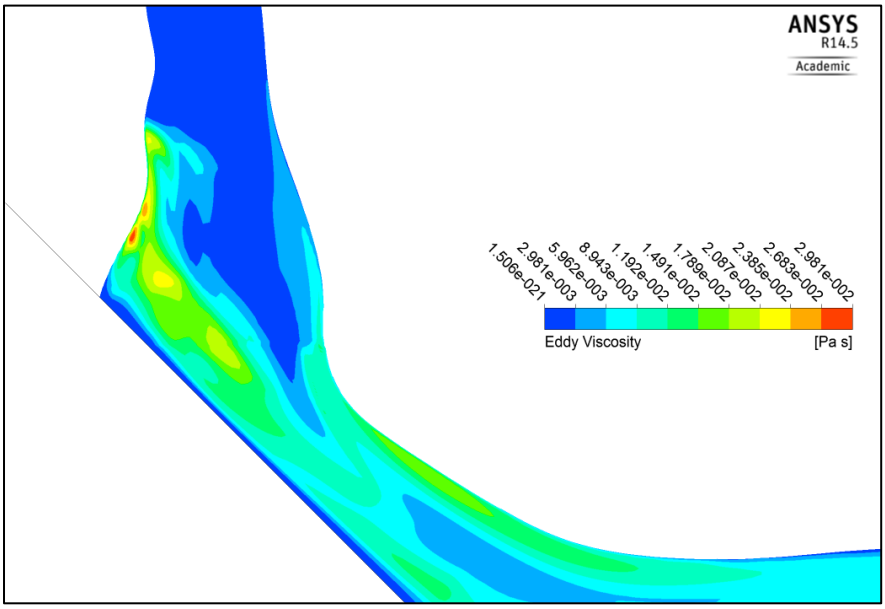

Figure 2-5 Eddy viscosity at the first impingement

The second phenomenon is the generation of roll waves during open channel flows. Bruno and McCready showed the mechanism of formation of roll waves on a horizontal liquid layer caused by a shearing effect of the gas flow on the liquid/gas interface [90]. The formation of the roll waves originates from slowly growing disturbances, which can more generally be compared to the

Kelvin-Helmholtz instability. This is best shown on Figure 2-6. The interface behavior and stability can best be expressed in terms of velocity potential, as shown in equation (47) where subscript *n* indicates the phase.

$$\nabla\phi_n = U_n \tag{47}$$

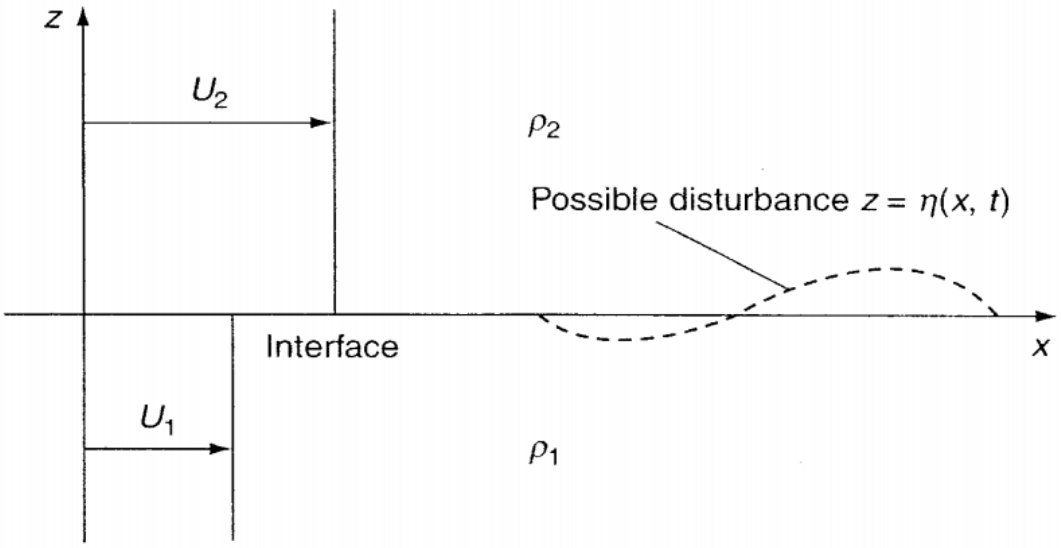

Figure 2-6 Velocity shear across a density interface with $\rho_1 > \rho_2$ [91]

By substituting into the incompressible continuity equation, equation (7), the Laplace equation is obtained:

$$\nabla^2\phi_n = 0 \tag{48}$$

Flow is then decomposed into two states: steady basic flow and the time dependent perturbation as follows:

$$\widetilde{\phi_n} = \phi_n + \phi_n' = U_n x + \phi_n' \tag{49}$$

By substituting equation (49) into equation (48), we get:

$$\nabla^2\phi'_n = 0 \tag{50}$$

Since disturbances die out far from the interface, then:

$$\nabla^2 \phi_1' \to 0 \; as \; z \to +\infty \tag{51}$$

$$\nabla^2 \phi_2' \to 0 \; as \; z \to -\infty \tag{52}$$

By evaluating the flow at the interface, one can surmise that the interface velocity matches the vertical velocities of both phases. Thus:

$$At \; z = \eta: \quad w_i \equiv \frac{\partial \tilde{\phi}_n}{\partial z} \approx \frac{d\eta}{dt} = \frac{\partial \eta}{\partial t} + u_n \frac{\partial \eta}{\partial x} \tag{53}$$

With an unsteady Bernoulli's equation, equation (54), and the Laplace's equation, equation (48), one can introduce a simple disturbance into the problem. In this case, a two-dimensional disturbance can be used to analyze the stability of the interface. This is expressed in equation (55), where *k* is the wavenumber, and real, and *σ* is the frequency, and complex.

$$At \; z = \eta: \quad C_n = \rho_n \frac{\partial \phi_n}{\partial t} + \frac{\rho_n}{2} \; |\nabla \phi_n|^2 + P_n + \rho_n g \eta \tag{53}$$

$$(\eta, \phi_n') = \left(\hat{\eta}, \hat{\phi}_n\right) e^{i(kx - \sigma t)} \tag{54}$$

The solutions of equation (50) must then take the form expressed in equation (55). By using equation (53), one can determine the coefficients *A* and *B*, which can then be substituted into the unsteady Bernoulli's equation. The result is a quadratic equation, where the solution of σ is shown in equation (56).

$$\hat{\phi}_1 = A e^{-kz} \; and \; \hat{\phi}_2 = B e^{kz} \tag{55}$$

$$A = i\eta_o \left(U_1 - \frac{\sigma}{k}\right) \; and \; B = i\eta_o (U_2 - \sigma k) \tag{55}$$

$$\sigma = \frac{\rho_1 U_1 + \rho_2 U_2}{\rho_1 + \rho_2} \; \pm \sqrt{\frac{\rho_1 \rho_2 (U_1 - U_2)^2}{(\rho_1 + \rho_2)^2} - \frac{\frac{g}{k}(\rho_1 - \rho_2)}{\rho_1 + \rho_2}} \tag{56}$$

For the instability to grow, σ must also have an imaginary part, thus the result under the square root must be negative for the flow to be unstable. By rearranging the expression underneath the square root, one can generate the following stability condition:

$$(U_1 - U_2)^2 > \frac{g(\rho_1^2 - \rho_2^2)}{k\rho_1\rho_2} \tag{56}$$

The following expression can give two insights towards the production of roll waves on the HSBC caster. First, the likely situation where $U_1 \neq U_2$, where the two velocities represent the velocity of the atmosphere and the liquid melt respectively, will be unstable for short enough wavelengths since the wave number *k* is inversely proportional to the wavelength. In other words, the presence of small waves will always be present unless the velocity or density difference is minimized. As for the case of the HSBC caster, the velocity difference is the only control, as determined by belt speed, and thus can be used to control the stability of the liquid melt. As the numerical results have shown the generation of the perturbation begins at the first impingement, as caused by the oscillating behavior of the flow, it is important to encourage conditions that promote fluid stability. In other words, by minimizing the velocity gradient, one can promote wave decay and kill the instability prior to solidification.

The next phenomenon is the effect of the Froude number. As the liquid melt moves down the inclined delivery system, the flow can be compared to an inclined, open channel flow. Freeze *et al.* reviewed the effect of the Froude number on surface waves in turbulent, open channeled water flows [92]. They showed that as the Froude number grows, the stabilizing effect of gravity is reduced and as a result, an increase in turbulent structures on the flow. This leads to more disturbance on the free surface. The Froude number is expressed in equation (57), where u_o is the characteristic flow velocity, g_o is the gravitational component into the plane and l_o is the characteristic length. In the case of the HSBC caster, as the inclination angle, θ, grows, the gravitational component becomes smaller, resulting in an increase in the *Fr*. This in turn will lead to increased turbulent activity and finally the likelihood of surface disturbances.

$$Fr = \frac{u_o}{\sqrt{g_o l_o}} \tag{57}$$

In the following problem, it was determined that the Froude number was 7.52 along the inclined plane and 6.32 along the moving belt, both of which are in the regime of supercritical flows. This transition will create a regime of relatively higher turbulence at the second impingement (meniscus point). This is shown in Figure 2-7, where the second impingement is a regime of high turbulence kinetic energy due to this transition. This high turbulence regime will be a likely location for air entrapment within the fluid which may further result in circular pores within the liquid melt [15].

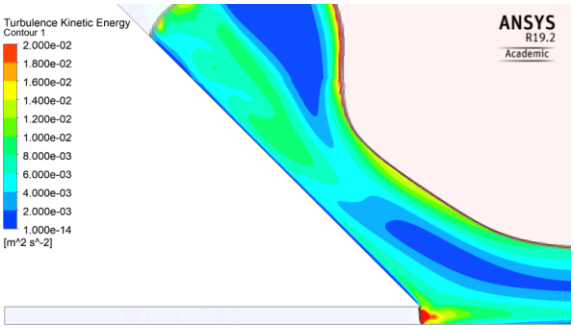

Figure 2-7 Turbulence kinetic energy at the first and second impingement

Pressure contours along the inclined ramp is shown in Figure 2-8. Noticeably two regimes of high pressure exist at the first and second impingement. As shown in Figure 2-9, the velocity magnitude decreases significantly at both locations, resulting in this high relative pressure. The velocity of the liquid melt along the melt quickly reaches a uniform velocity along the thickness of the liquid melt at the end of the numerical regime.

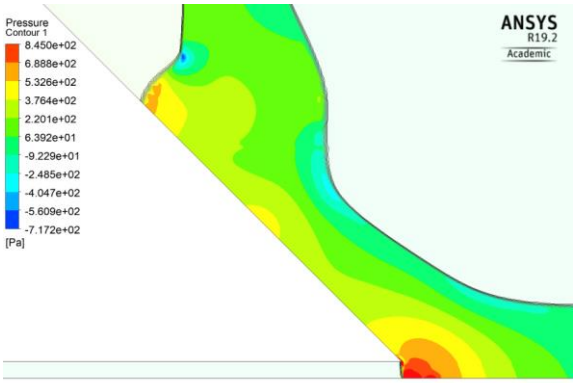

Figure 2-8 Pressure contour at the first and second impingement

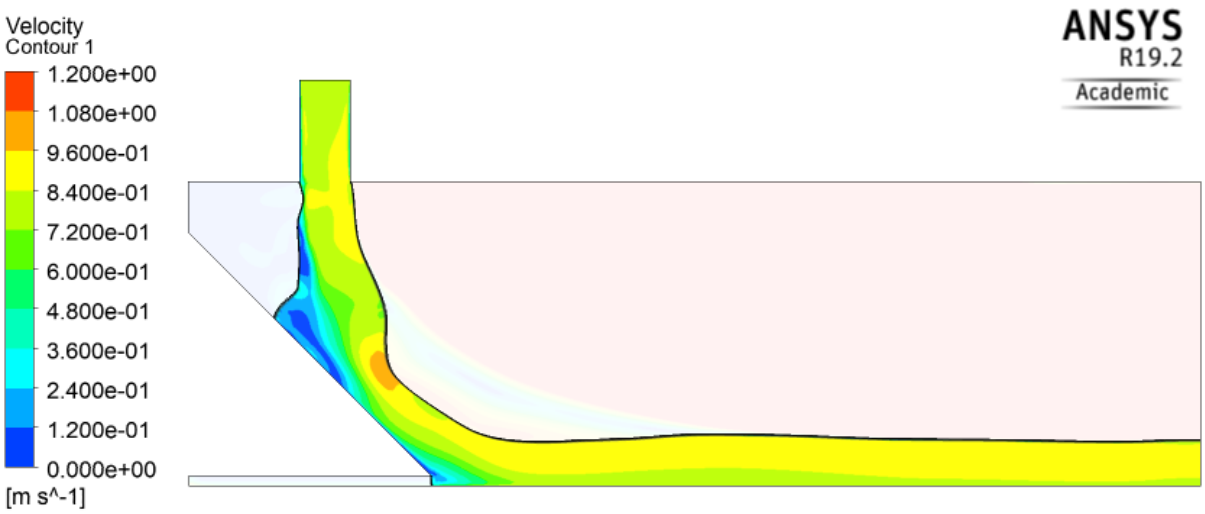

Figure 2-9 Velocity magnitude contours

It is important to note that a solidification model was not used in the present numerical models. Had a solidification model been used, a source term would have been added to the momentum equations in relation to the liquid/solid ratio within each node. With a lower liquid/solid ratio, implying higher solidification, the source term will inhibit flow, minimizing turbulent activity and thus may result in reduced surface instability within the fluid flow.

2.5 Heat transfer of AA2024 during the HSBC process

The HSBC caster has, in place, thermocouples located in the five water cooling sections underneath the belt. Unfortunately, these show little temperature change during casting experiments as they are located within the high velocity bulk water flow systems under the belt. They are not aimed at measuring temperature profiles along the lower surface of the steel belt. As such, the moving belt was modelled as a steel wall of known thickness and thermal properties. The bottom boundary condition of the solid wall was given a constant temperature boundary condition of 25°C, with the solid surface modelled by thermal conduction. The resulting temperature isotherm contours, as shown in Figure 2-10, show the cooling behavior of AA2024 on moving belt. As expected, the melt cools in a relatively uniform manner along the belt length, with the disturbances associated to the hydraulic jump and resulting flow behavior along the belt. This is best represented by the cooling behavior at different thicknesses shown in Figure 2-11.

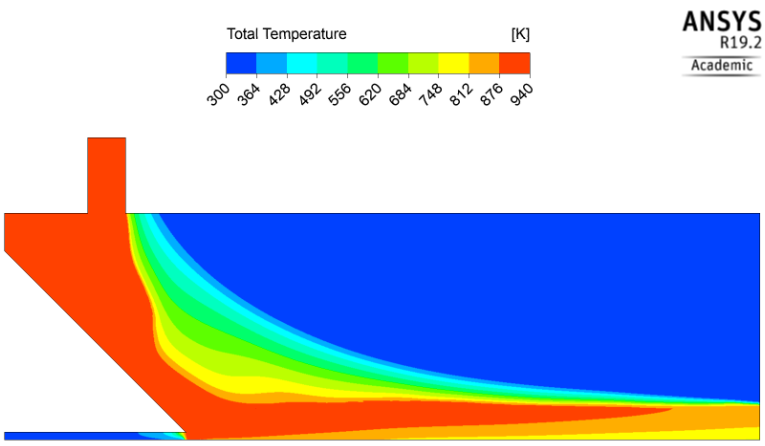

Figure 2-10 Temperature isotherm contours

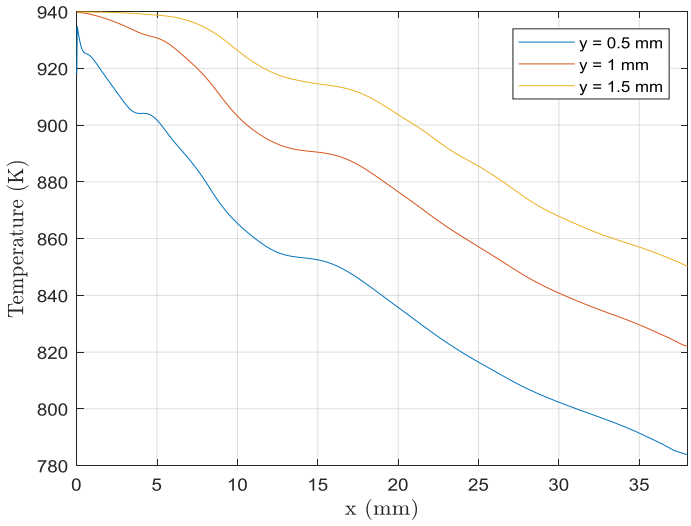

Figure 2-11 Strip temperature evolution at different thicknesses over the length of the simulation domain

The numerical model showed a maximum heat flux of 17.8 MW/m^2, as shown in Figure 2-12, with a similar heat flux profile to numerical models presented by Ge *et al.* [25]. It is important to note that the numerical model presents an idealized heat flux condition, with perfect maximum contact between liquid melt and the moving belt with no surface roughness. As shown by Guthrie *et al.*, the interfacial heat fluxes are dependent on surface quality and as the HSBC process involves a

graphite coating on the moving belt, it is expected that the true heat flux will be lower by 25-35%, although the heat flux profile will be maintained [2].

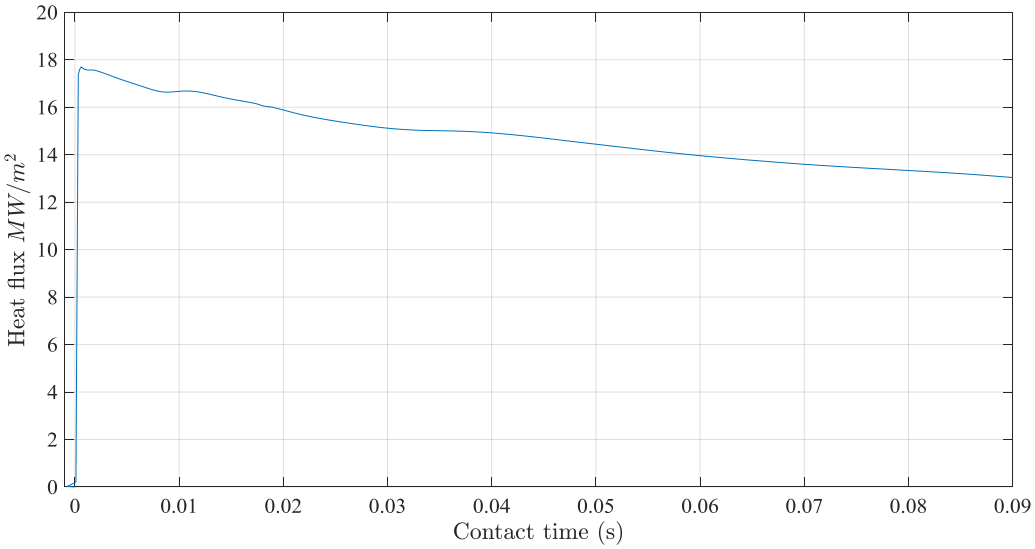

Figure 2-12 Interfacial heat flux of AA2024 as determined by the present CFD model

The present numerical models provided insight towards the flow behavior of AA2024 using the HSBC process. Flow instability was shown to be created by an oscillating flow occurring at the stagnation point. By using the Kelvin-Helmholtz instability, one can promote wave decay by minimizing the velocity gradient between the air and the liquid melt. Furthermore, by reducing the Froude number, the turbulent activity of the melt can be reduced and thus further promoting surface stability in the final cast product.

Chapter 3 HSBC Simulator and HSBC Pilot-Scale Machine Design and Procedure

In this chapter, a discussion of the HSBC Simulator and the HSBC Pilot-Scale Machine focusing on the designs and procedures is presented. This will include an explanation on the data acquisition, alloying and melting of AA2024, casting preparations and finally casting procedure. As previously explained, the experimental procedure will be performed in two stages: first using the HSBC Simulator and second using the HSBC Pilot-Scale Machine.

3.1 HSBC Simulator Design and Operation

For simulator scale experiments, an alumina based refractory lining, Metal Kast 90, was used to line the internal section of a simulator specific tundish, as shown in Figure 3-1. A porous refractory is then used for an easily replaceable nozzle slot. A sandblasted pure copper belt was used as the moving belt, with its movement propelled using a spring loaded system at a velocity of 0.8 m/s. The full schematic of the HSBC simulator is shown in Figure 3-3 and the HSBC simulator and induction furnace are shown in Figure 3-3. T-type grounded thermocouples were placed inside the pure copper belt to measure temperature evolution within the solid. Using DASYLab data acquisition software and an instruNet i555 system, temperature data was produced, filtered and measured at a rate of 16Hz. The data acquisition routine is shown in Figure 3-4. This temperature evolution is then used to determine the interfacial heat flux using a second order regularization IHCP code, as described in Chapter 1.

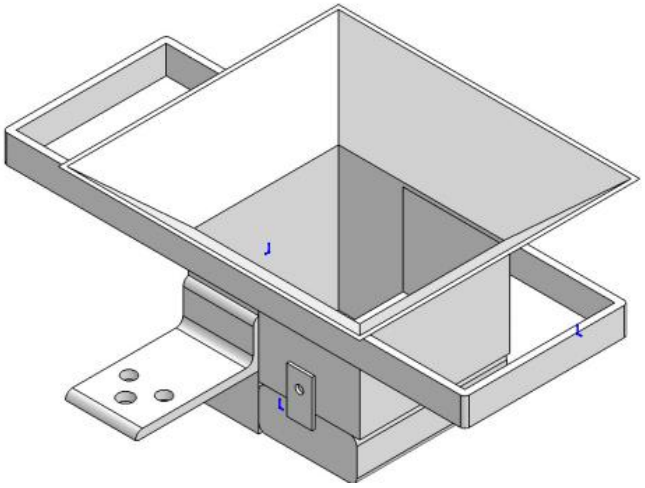

Figure 3-1 Simulator specific tundish, as drawn by A. Panicker, K. Selim and X. Zhu

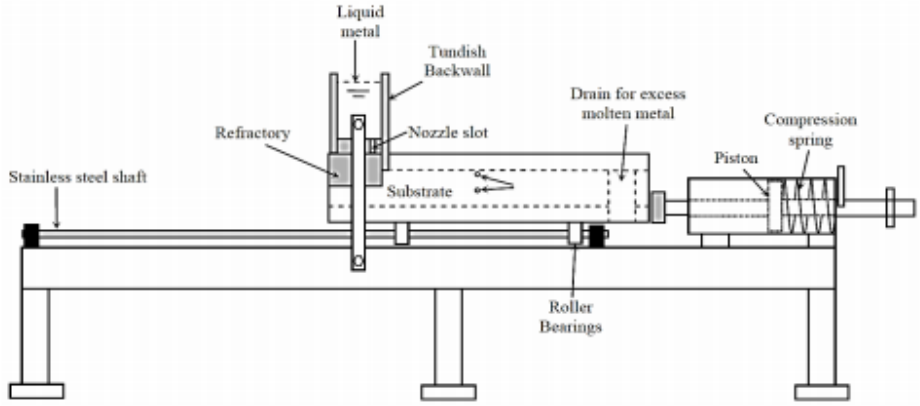

Figure 3-2 Full schematic of the HSBC Simulator [4]

Pure aluminum, Al-25Mg, Al-25Mn and Al-50Cu ingots were cut, measured and alloyed using a small-scale induction furnace inside a magnesia-based crucible to produce AA2024. 600g of AA2024 was then produced using the induction furnace. Temperature was raised slowly, with the pure aluminum melting first, to minimize effects of thermal shock on the crucible and oxidation of the melt. To further minimize the effects of oxidation, an argon shroud was used during melting. Due to the purity of the argon (99.9%), special attention was made to the flowrate of the shroud to ensure the heavier argon gas rests above the melt with minimal disturbance and to ensure that additional oxygen does not enter the liquid melt.

Figure 3-3 Induction furnace with the HSBC Simulator

Figure 3-4 Data acquisition routine for Simulator scale experiments

To minimize heat loss in the tundish, a natural gas burner was used to preheat the tundish, the refractory lining and the nozzle slot. Once the AA2024 was melted and alloyed, the liquid melt was poured into the tundish and settled before the moving belt was propelled. Temperature was also measured in the tundish to determine the superheat just before casting. To ensure a consistent flow with minimal turbulence, a stopping block was placed underneath the tundish to allow the liquid melt to reach a certain metal head in the tundish. Once the AA2024 was poured from the

crucible into the tundish completely, the belt was propelled forwards, causing the stopper block to move downstream and the melt to be released to flow freely onto the copper substrate. These experiments provided an understanding of the interfacial heat flux and the viability of the HSBC process producing AA2024.

3.2 HSBC Pilot-Scale Design and Operations

An HSBC pilot-scale machine was used to produce 180mm and 200mm wide AA2024 strips, as shown by a delivery system schematic in Figure 3-5 and by the pilot scale machine in Figure 3-6. For HSBC pilot-scale experiments, a newly designed tundish delivery system, made of a material an iron-nickel based alloy Invar, was built to hold the refractory lining, to produce wider strips in comparison to previously produced 100 mm wide strips. Due to the lower coefficient of thermal expansion, Invar was deemed appropriate for the high temperature applications. The design of the widened tundish is shown in Figure 3-7.

Water pressure was managed at 50 psi to promote a high cooling rate without causing water leakage onto the surface of the moving belt. To evaluate superheat temperature and the effectiveness of the water cooling underneath the belt, a system of thermocouples was set up with the HSBC machine. Six K-type grounded thermocouples were placed in the launder to help measure the superheat of the liquid melt and to manage the temperature of resistance preheaters placed over the launder. 12 J-type grounded thermocouples were set underneath the moving belt to measure the temperature underneath the belt as well as to measure the water temperature leaving the belt cooling system. The data acquisition routine utilized the same routine as that of the simulator experiments (Figure 3-4).

Nozzle slots of 3mm thickness were casted using Metal Kast 90. To improve the surface quality of the refractory material along the delivery launder, a boron nitride (BN) coating was used. A 45° inclined ramp was used as the delivery system, matching the dimensions used for the numerical model. Like the simulator scale experiments, a stopping system was used to minimize turbulence and allow for a consistent metal head before casting begins. In the case of the pilot-scale experiment, a stopper road was built and used to allow for a metal head height of 4 cm before casting. Using a mass balance, a correlation between metal head and belt velocity on the strip

thickness can be made. This is shown in Figure 3-8, which has shown good correlation to previous HSBC experiments. 180mm and 200mm nozzle slots were used for the casting of AA2024.

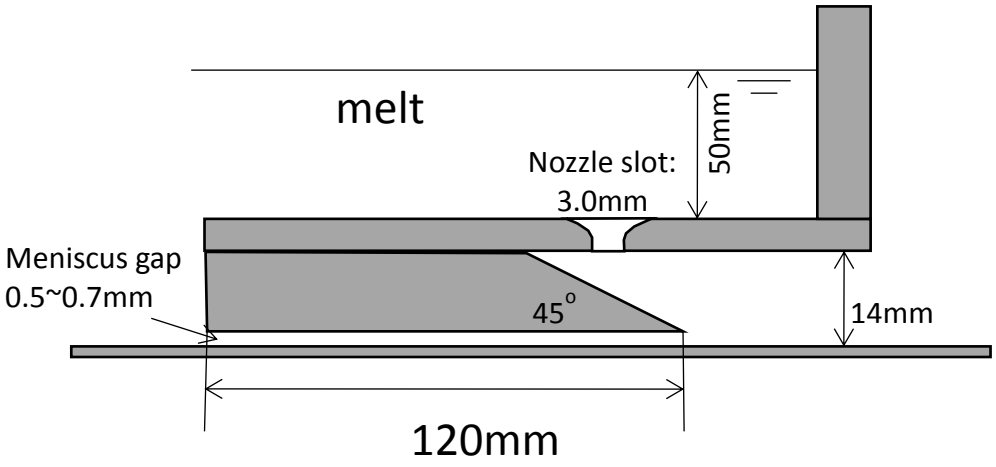

Figure 3-5 Delivery System Schematic

Figure 3-6 HSBC pilot-scale machine located at the Stinson Laboratories

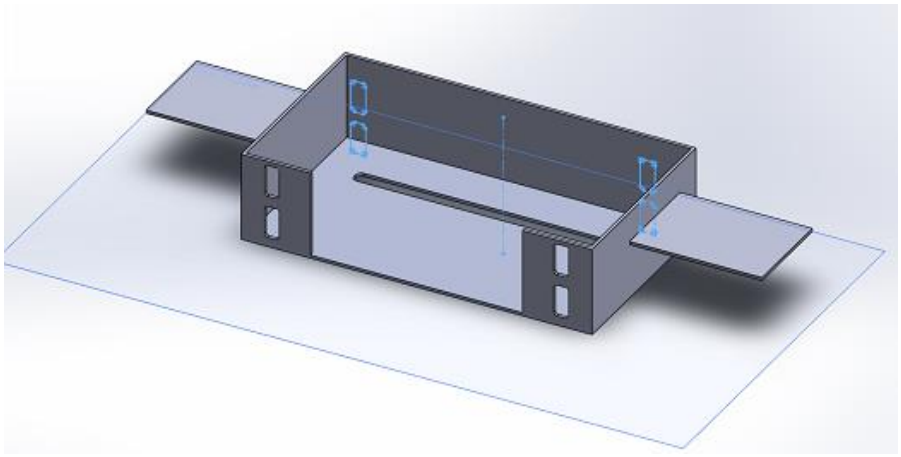

Figure 3-7 New widened tundish for the HSBC pilot-scale caster

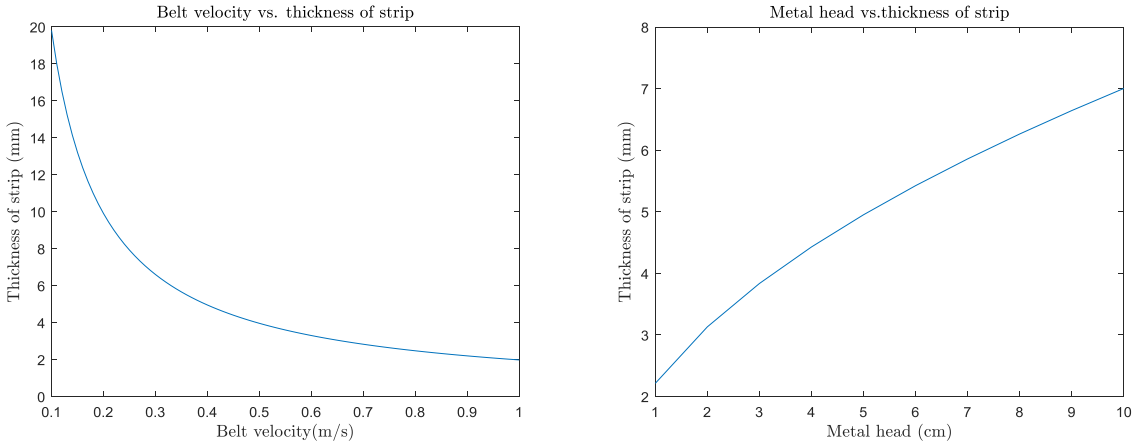

Figure 3-8 Belt velocity vs. the thickness of the strip at a metal head of 5 cm (Left) and metal head vs thickness of strip at a belt speed of 0.4 m/s (Right)

To manage the metal head height, a mass balance was also used to dictate piston plunging speed. Depending on the metal head, the width of the nozzle, the belt speed and the desired strip thickness, the plunging speed would be optimized to ensure a consistent flow. To prevent solidification of aluminum onto the piston and reduce the wettability of the piston surface, a BN coating was used.

As previously discussed, a graphite coating has been shown to improve the bottom surface quality of strip products and thus was used in the following experiments. Due to the large freezing range of AA2024, a belt speed of 0.33 m/s was used to minimize the risk of incomplete solidification at the end of the moving belt and before the conveyor belt. As the moving belt is the primary source

of cooling due to the high-pressure water-cooling system, it is important to have a completely solid strip at this point of the experiment in order to minimize risk of cracking and breaking of the strip.

Alloying and melting of AA2024 operated in a similar fashion to the simulator scale experiments. 45 kg and 75kg of AA2024 was alloyed and prepared using a 300lb Dura-Line Inductotherm induction furnace for casting of 180 mm and 200 mm wide strips respectively. To preheat the induction furnace, a gas burner was used to heat the furnace lining temperature for 1.5 hours to achieve a temperature near melting temperature of AA2024. Pure aluminum was first melted to create a liquid melt pool. Due to the higher melting temperature, Al-25Mn was added next before Al-50Cu and Al-25Mg were added at the end. Al-5Ti-1B grain refiner was added to promote an equiaxed, refined microstructure in the solid strip. The additions of alloying elements for a 75 kg cast of AA2024 are shown in Table 3-1. An argon gas shroud was used to minimize oxidation. At the end of melting, the liquid melt was degassed using argon gas prior to casting to minimize hydrogen content.

Table 3-1 Additions of alloying elements for 75kg of AA2024

Pure Al	Al-50Cu	Al-25Mn	Al-25Mg	Al-5Ti-B
66.24 kg	7.11 kg	2.00 kg	4.74 kg	110g

3.3 Experimental Analysis Techniques

Interfacial heat flux values were determined using the temperature-time evolution data from the HSBC Simulator. A second order regularization method, as discussed in Chapter 1, was used to determine the heat flux values. A modified Fortran code first presented by Tavares and modified for a rectangular coordinate system was used to solve the interfacial heat flux values using

temperature profiles measured at two depths in the HSBC Simulator moving interface [87]. The Fortran code used is shown in Appendix I.

Casting behavior was determined using cameras placed in two locations during casting. One camera was placed facing the nozzle to evaluate the fluid flow behavior at the start of casting. This will give information regarding the stability of the flow and give information on any causes of strip defects. The second camera was placed facing the end of the belt to show the strip exiting behavior and to evaluate the strip quality after solidification.

Strip products were evaluated for both macro and micro properties. Strip thicknesses and widths were measured over several cross sections to determine uniformity along the strip product. Surface quality evaluations were performed using a 3D Nanovea profilometer. To ensure an accurate measurement with little noise, a low wavelength (100μm) laser was used to minimize "non-measured" points and to thus improve measurement accuracy. 3mm x 3mm surface areas were measured on both the top and bottom surface of each pilot-scale casted strip. Surface height fluctuation measurements and 2-D distributions were created using the Surface Profilometer by Nanovea Inc.

For microstructure analysis, AA2024 samples were cut along the cross section at seven points along the width of the sample before being ground and polished. Samples were then analyzed using an optical microscope at three different cross sections: near the bottom of the strip, the middle of the strip and near the top of the strip. Using ImageJ software, an analysis of porosity was performed for each sample. AA2024 samples were then electropolished and etched using a 2% perchloric acid and reagent alcohol mixture before being analyzed once again using ImageJ software to

measure grain size. Measurements were made over several position on each sample to ensure a large enough data distribution.

To evaluate the correlation between grain size and porosity to the vertical and horizontal position on the strip, Python libraries including Pandas, Numpy and Matplotlib were used to visualize the distribution. The Python script used is shown in Appendix II.

Mechanical properties were also evaluated using a Vickers microhardness test and a 1mm diameter shear punch test to evaluate hardness and tensile strength respectively. Samples were prepared using the as-cast strips produced by the HSBC pilot-scale machine, with hardness tests being performed on both the top and bottom surface. In addition, shear punch samples of 0.7 mm thickness were prepared, with measurements performed at several locations. Shear stress and strain were measured using equations (58) and (59), where P is the load, r_{avg} is the average radius of the die punch, t is the thickness of the sample and d_f is the displacement. Yield tensile stress σ_{ys} and ultimate tensile stress σ_{us} were determined using the yield shear stress τ_{ys} and ultimate shear stress τ_{us} and relationship in equation (60).

$$\tau = \frac{P}{2\pi r_{avg} t} \tag{58}$$

$$\epsilon_{eff} = \frac{d_f}{t} \tag{59}$$

$$\sigma_{ys} = 1.77\,\tau_{ys} \quad and \quad \sigma_{us} = 1.8\,\tau_{us} \tag{60}$$

Chapter 4 Results and Discussion

In this chapter, the results from the simulator and pilot-scale HSBC experiments are shown. Interfacial heat flux measurements are performed using the HSBC simulator while characteristic macro- and micro-properties of the strip product are evaluated from products of the HSBC pilot-scale machine. Casting behavior will be presented and discussed with respect to the fluid flow model presented in Chapter 2. Surface quality evaluations and strip measurements are presented to help address macro-analysis while grain size distributions and porosity distributions are presented for addressing micro-analysis aspects of the strip products. Mechanical properties including hardness tests and tensile behavior of as-cast AA2024 are also presented.

4.1 Macro Properties of AA2024 using the HSBC Simulator

Experiments using the HSBC simulator presented an opportunity to evaluate fluid flow behavior and heat transfer of AA2024 using the HSBC process. The strip exhibited consistent strip qualities on reaching steady state. This is best shown in Figure 4-1 and Figure 4-2. Both steady state segments of the HSBC simulator strips showed excellent surface and side qualities with no distinct surface defects. The bottom surface especially showed very little dimpling beyond the centreline of the strip, owing to the thick graphite coating used on the copper belt. Similarly, the top surface showed a small indentation along the centreline of the strip with few indications of roll wave formation along the strip surface. Strip width shrunk 20% in comparison with nozzle width, from 60 mm width in the nozzle to 48mm width for the strip, while the thickness was measured to be 2.25 mm. This is summarized in Table 4-1.

Figure 4-1 Top surface of AA2024 strip produced by HSBC simulator

Figure 4-2 Bottom surface of AA2024 strip produced by HSBC simulator

Table 4-1 HSBC Simulator Parameters and Strip Macro properties

Casting Speed	Nozzle Dimensions	Inclination Angle	Ramp Length	Strip Width	Strip Thickness
0.8 m/s	4.5 mm x 60 mm	30°	30 mm	48 mm	2.25 mm

As initially discussed in Chapter 2, surface instability is governed by the velocity gradient at the liquid melt/air interface as well as the Froude number along an inclined plane. Specifically, a longer inclined plane, as defined by the length scale in the equation (57), would reduce the Froude number and minimize surface instabilities. The problem arises with the shrinkage along the width of the strip that was noticeable during several simulator scale experiments using AA6111, AA2024 and Advanced High Strength Steels (AHSS). As the exit fluid flow is at maximum at the center of the nozzle, where the velocity profile adopts a parabolic profile, it can therefore be expected that the liquid will maintain a similar velocity profile down the ramp. Due to this, the strip will undergo shrinkage both vertically and across the belt width, to maintain mass conservation along the length of the ramp. Given this, the width of the fluid will decrease.

To minimize this, one can use a shorter ramp to allow for the liquid melt to quickly reach the moving substrate or moving belt. Once the fluid reaches the moving belt, the fluid will be pulled along the belt at the same speed, assuming no slip conditions at the wall. This would result in less time for the fluid to shrink due to this parabolic velocity profile along the ramp, ultimately resulting in less fluid shrinkage. This is noticeable in previous pilot-scale casts where shorter ramp lengths (17 mm) were used and strip shrinkage was non-existent.

4.2 Heat Transfer and Micro Properties of AA2024 produced using the HSBC Simulator

The interfacial heat flux was calculated, and the results are shown in Figure 4-3. A maximum heat flux of 11.8 MW/m^2 was achieved, being approximately 6 MW/m^2 lower than that achieved by the numerical model. The lower heat flux achieved in the HSBC Simulator in comparison to the numerical model reflects the imperfect contact between the copper belt and the liquid melt. Due to the sandblasted surface, graphite coating and the interfacial air gap, the fluid did not maintain perfect contact and thus the maximum heat transfer portrayed in the numerical model was not achieved. The heat flux profile, however, exhibits a very similar profile to previous HSBC Simulator experiments with a sudden peak, occurring within 0.1, before levelling at approximately 1.3 MW/m^2. This is in comparison to heat transfer rates occurring in DC casts, where heat fluxes can reach a maximum of 0.9 MW/m^2 [93], HSBC Simulator showed significantly higher heat transfer rates. This will play a large role in both improving castability of AA2024, improving microstructure as well as minimizing the size of constituent particles.

It is important to note that during preheating of the tundish using a gas burner, the flame exited through the nozzle and the heat reached the copper substrate. Due to this, the surface temperature of the copper substrate increased to temperatures of upwards of 120°C. Due to this high temperature on the surface of the belt, the heat removal by the belt would be less than the predicted numerical model due to the reduced temperature gradient between the liquid melt and the substrate.

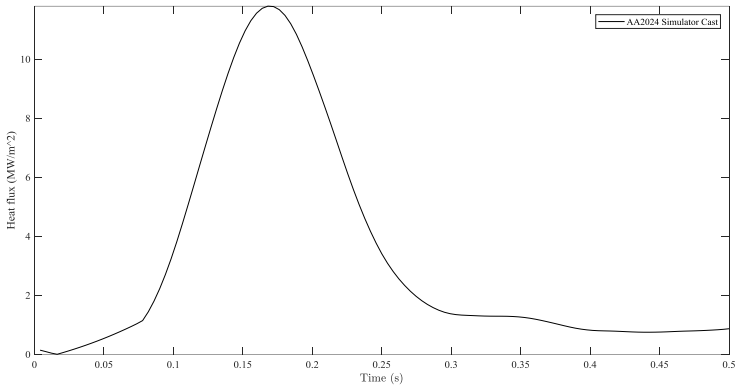

Figure 4-3 Interfacial heat flux of AA2024 using the HSBC Simulator

With regards to the micro properties of the strip, microstructure measurements were taken throughout the strip. Micrographs of the strip cross-section are shown in Figure 4-4. Since the strip was very thin (2.25 mm), there was very little variation in microstructure between the bulk and the bottom of the strip surface. A grain size average of 71.8 μm, with a standard deviation of 11.0 μm, was measured in the AA2024 strips. In addition, the refined structure showed an SDAS measuring 8.6 μm, with a standard deviation of 0.1 μm. The refined microstructure is representative of the high interfacial heat transfer rate achieved by the HSBC process and as a result shows promise especially towards scaling up to a pilot-scale machine.

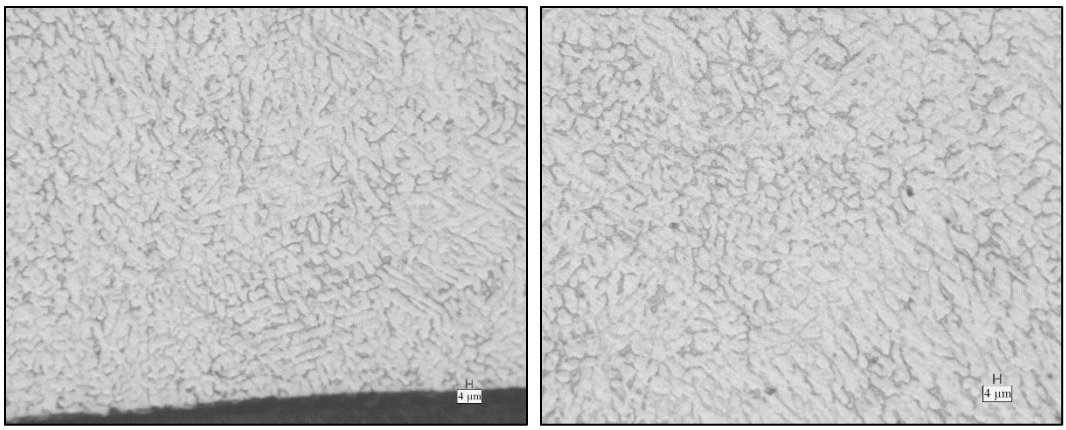

Figure 4-4 Micrographs at 200X magnification for the strip cross-section at the bottom (Left) and at the bulk (Right)

4.3 Casting Behavior of AA2024 using the Pilot-scale machine

Using the pilot-scale machine provided several insights towards the fluid behavior of AA2024 during casting. For the casting of 180 mm and 200 mm wide AA2024 strips, superheat temperatures of approximately 5°C and 15°C respectively were achieved at the nozzle. The steady state flow for the 180 mm strip is shown in Figure 4-5. The strip exhibited consistent edge and surface quality throughout the entire cast, showing roll waves along the surface. These "roll waves" perpendicular to cast direction remained consistent through the cast at a constant wavelength.

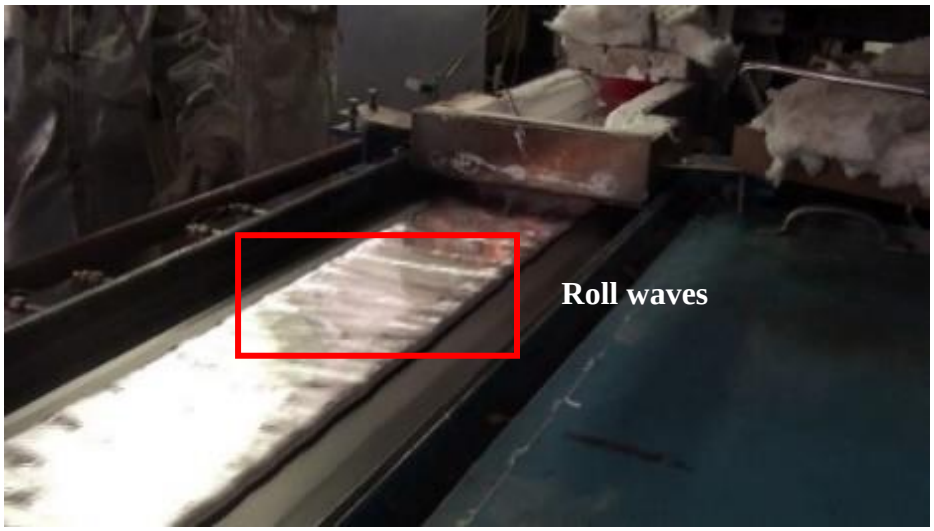

Figure 4-5 180 mm AA2024 strip during casting using the HSBC pilot-scale machine

Noticeably, the source of the instability appeared to occur from the oscillation of the fluid as well as along the edges of the strip at the first impingement. This is best shown by previous experiments conducted by Li *et al.* whom utilized a high speed camera to analyze fluid flow behavior using the same delivery system [94]. A high-speed image is shown in Figure 4-6 showing the fluid flow from the edge of the strip towards the center. This surface fluid flow accumulates and forms the roll waves that are apparent along the moving belt. A unique difference between the AA2024 cast and the casts performed by Li was the edge thinning phenomena occurring during the cast of 100 mm wide AA6111 strips [94]. This did not occur for either cast of AA2024.

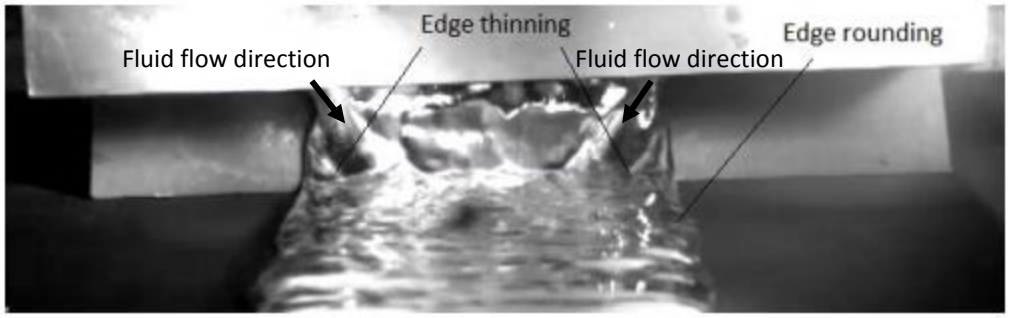

Figure 4-6 High speed camera image of the incline delivery system using the HSBC for 100mm wide strip [94]

For the cast of 200 mm wide AA2024 strip, at a superheat of 15°C however, the presence of "roll waves" were significantly less. As the superheat was higher and the width of the strip increased, the presence of roll waves was visually less, as shown in Figure 4-7. Compared to the cast of 180 mm wide strip, the flow from the edges towards the center was much less significant, resulting in the production of smaller "roll waves" that appeared to diminish along the belt length. Once again, the strip edges remained rounded and consistent along the strip length.

Figure 4-7 280 mm AA2024 strip during casting using the HSBC pilot-scale machine

The fluid flow during casting, however, was very susceptible to any disturbances downstream of the horizontal belt. During one cast, the strip was partially impeded by the bottom rolls of the pinch roller, causing a slight disturbance that carried upstream from the end of the belt towards the beginning of the belt. As a result, the strip quality was significantly changed. Side quality, as shown in Figure 4-8, and surface quality, as shown in Figure 4-9, suffered with both exhibiting instabilities along the edge and along the surface.

Figure 4-8 Edge instability produced by downstream disturbance

Figure 4-9 Surface instability produced by downstream disturbance

4.4 Macro-properties of strip products using the HSBC pilot-scale machine

A summary of the AA2024 strip macro-properties is shown in Table 4-2. The strip thickness measurements coincide with the relationships shown in Figure 3-8, where a thicker strip was produced due to slower casting speeds and higher metal heads. Both the 180 mm wide and 200 mm wide strip, as shown in Figure 4-10, exhibited consistent surface and edge quality. Noticeably, the roll waves created during the cast remained present in the final product, resulting in edge perturbations and surface streaks perpendicular to casting direction. The frequency of the surface streaks remained consistent, with a mean distance of 48 mm $\pm$ 4.1mm.

Table 4-2 AA2024 strip macro-properties produced by HSBC pilot-scale machine

Casting Speed (m/s)	Superheat (°C)	Metal Head (mm)	Nozzle Dimensions (mm x mm)	Inclination Angle (°)	Ramp Length (mm)	Strip Width (mm)	Strip Thickness (mm)
0.33	5	50	180 x 3	45	17	182	8.3
0.33	15	55	200 x 3	45	17	200	9.8

Figure 4-10 180 mm wide strip top surface (Left) and 200 mm wide strip top surface (Right), with casting direction from left to right

The bottom surface exhibited similar behavior, with a slight dimpling effect consistent with previous HSBC casts, as discussed by Li *et al.* [8]. This is shown in Figure 4-11, with thin and long shaped dimples perpendicular to cast direction existing on the surface.

Figure 4-11 180 mm wide strip bottom surface (Left) and 200 mm wide strip bottom surface (Right), with casting direction from left to right

Surface profilometer measurements were performed for both the 180mm wide strip and the 200 mm wide strip. 2-D height distributions for both the 180 mm wide strip and the 200 mm wide strip on the top and bottom surfaces are shown in Figure 4-12, with the casting direction in the y-direction. With regards to the top surfaces of both casts, it is clear that surface waves exist for the 180 mm wide strip. On the other hand, even with visual streaks present on the surface, the surface is much more uniform for the 200 mm wide strip. It appears that the superheat temperature can play a distinct impact on the surface quality of the product.

This can be further explained by the Kelvin-Helmholtz instability discussed in Chapter 2. The surface roll waves must decay prior to solidification in order to minimize the surface defects in the final product. If the surface roll waves are present at solidification, as in the case in the 180 mm wide strip, the final product will exhibit larger surface roughness. Due to the lower superheat in

casting the 180 mm wide strip, the final product solidified sooner and thus the rolling waves did not decay in time.

With regards to the bottom surface, surface indentation remains present in both casts, as shown by both Figure 4-12 and Figure 4-13. In both cases, the surface indentation pattern appeared to be very similar in size, with more indents in the 180 mm wide casting in comparison to the 200 mm wide casting.

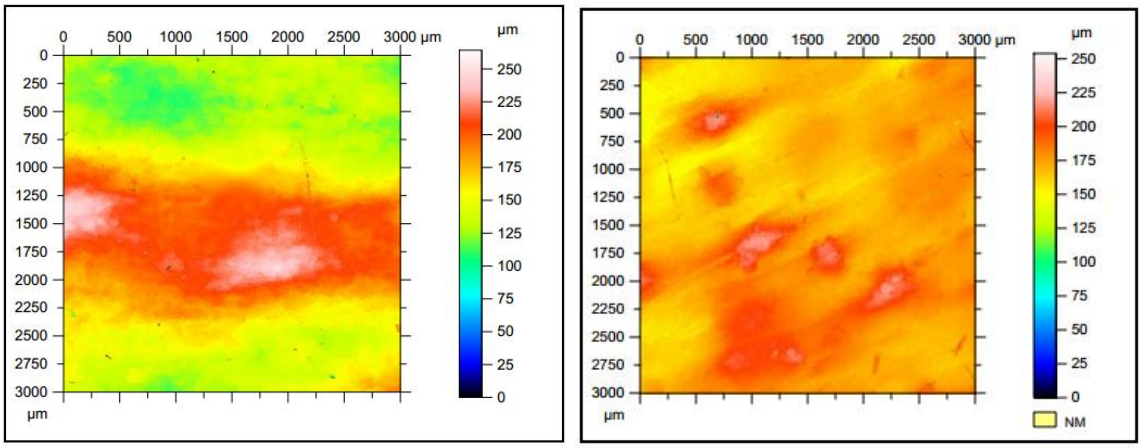

Figure 4-12 2-D surface profilometry analysis for 180 mm wide surface: top surface (Left) and bottom surface (Right)

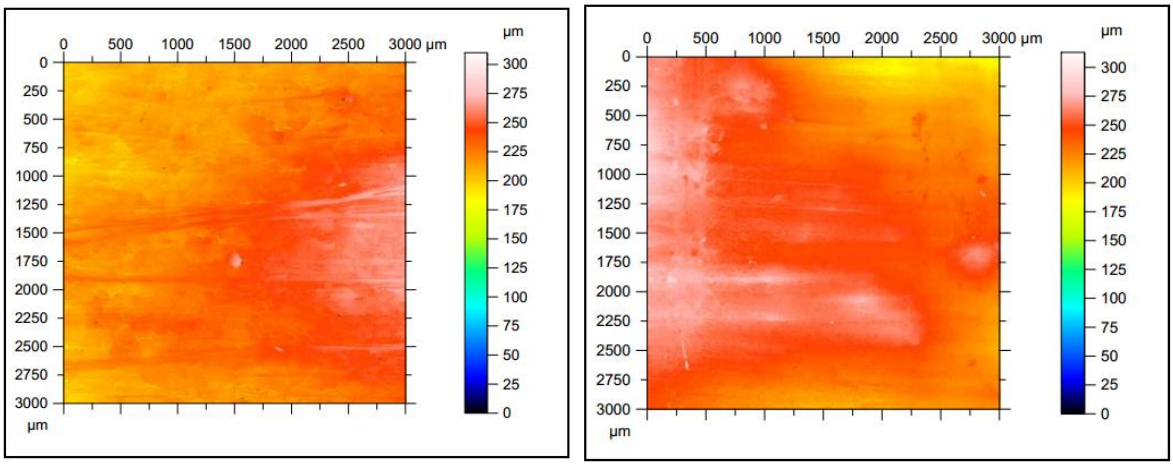

Figure 4-13 2-D surface profilometry analysis for 200 mm wide strip: top surface (Left) and bottom surface (Right)

To better understand the surface roughness behavior, surface height fluctuation measurements were made along the length and width of the casting strip. Top surface measurements for 180 mm wide and 200 mm wide strips are shown in Figure 4-14 and Figure 4-15 respectively. Surface height fluctuations along the width of the strip are minimal, with maximum height fluctuations of 47.2 and 58.7 µm for the 180 mm and 200 mm wide strips respectively. Noticeably, in the case of the 180 mm wide strip, the roll waves present can be shown to have a maximum height fluctuation of 121 µm and wave length of 2700 µm. For the 200 mm wide strip, the surface height fluctuations show no dependence along either direction, with nearly an identical max height fluctuation along the length of the strip (56.4 µm).

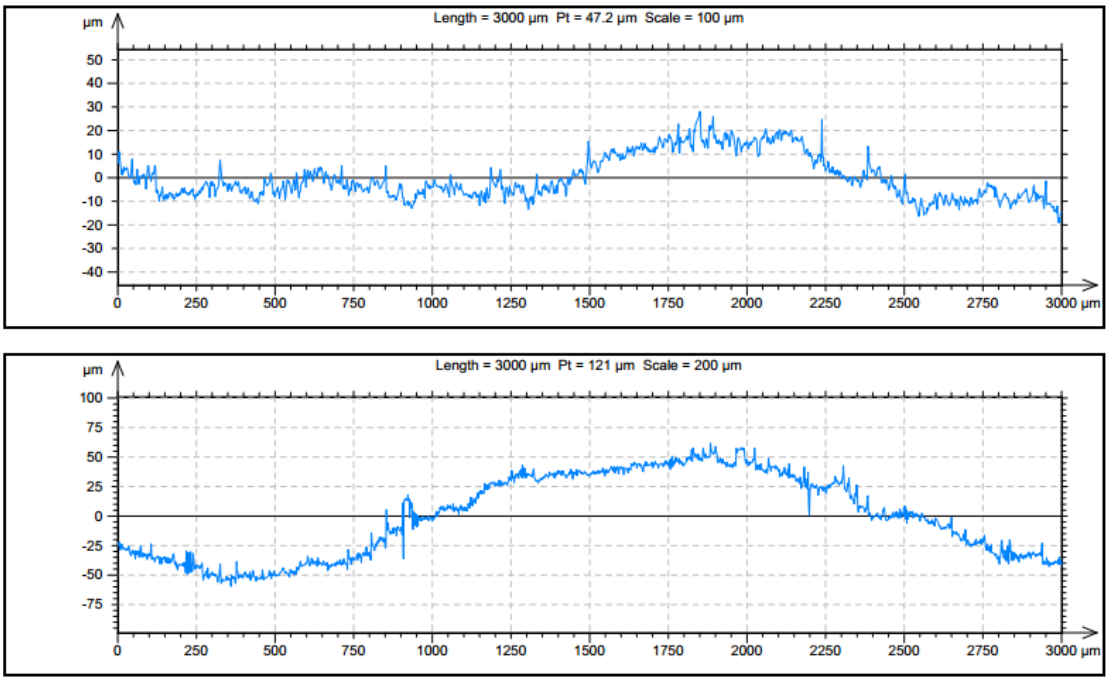

Figure 4-14 Surface height fluctuation measurements of the top surface of a 180 mm wide strip along width of strip (Top) and along length of strip (Bottom)

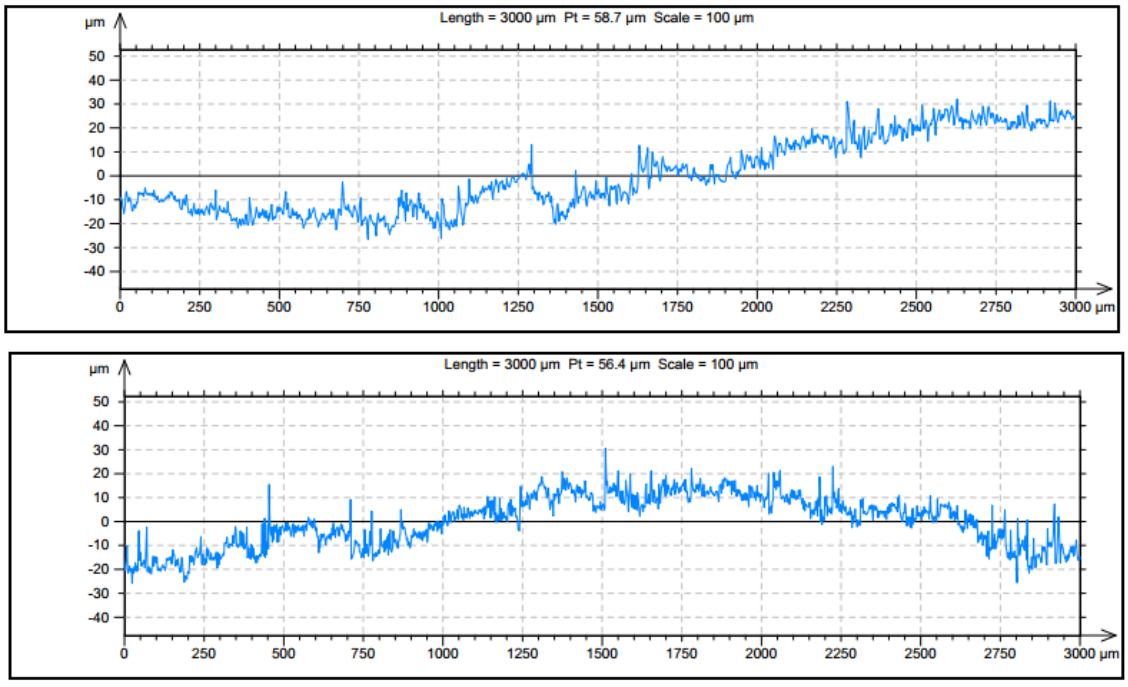

Figure 4-15 Surface height fluctuation measurements of the top surface of a 200 mm wide strip along width of strip (Top) and along length of strip (Bottom)

Bottom surface measurements are shown in Figure 4-16 and Figure 4-17 for 180 mm and 200 mm wide casts respectively. Measurements were taken along the length and width of the strip along the center of the strip surface. Indentations were measured to be have a size of 300 μm in length and 25 μm in depth. With regards to the bulk roughness, in both casts the surface roughness remains very consistent, with max fluctuations of 39.1 μm. With respect to previous HSBC experiments, the bottom surface remains to be consistent in terms of surface indentation and roughness.

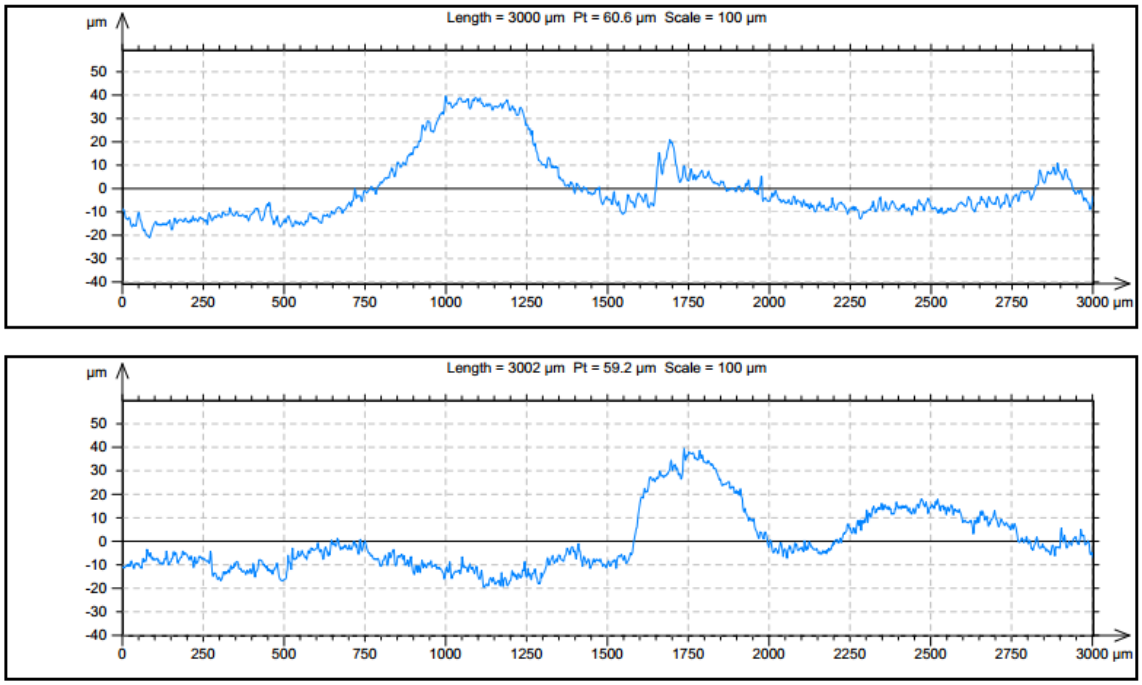

Figure 4-16 Surface height fluctuation measurements of the bottom surface of a 180 mm wide strip along width of strip (Top) and along length of strip (Bottom)

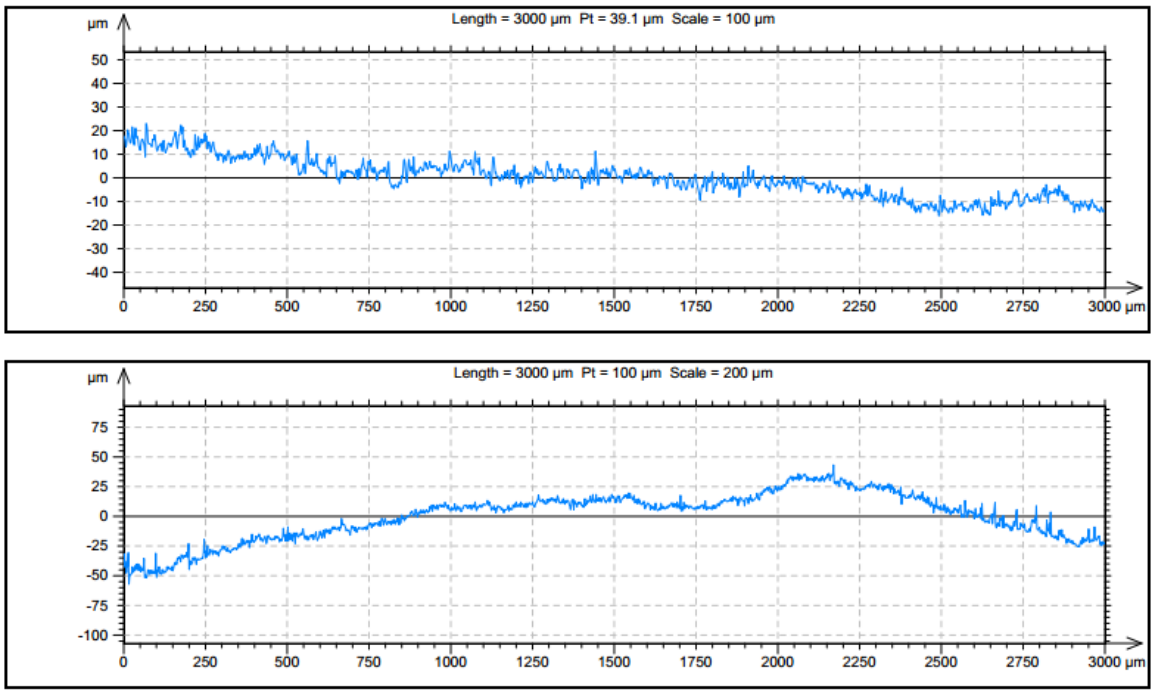

Figure 4-17 Surface height fluctuation measurements along the bulk of the surface

4.5 Micro-properties of AA2024 strip products using the HSBC pilot-scale machine

Porosity and grain size measurements were made on a typical cross-section of the strip, shown by Figure 4-18. Note that position is position from edge towards the centre of the strip and vertical height is measured from the base of the strip to its top. A summary of both measurements is shown in Table 4-3, showing mean, standard deviation and a summary of the distribution. As shown, grain size is consistent among both casts, exhibiting a mean grain size of 53.9 µm and 56.81 µm for the 180 mm wide and 200 mm wide strip respectively. The histogram of grain size for 200 mm wide strips is shown in Figure 4-19, representing a clear normal distribution. Due to the large standard deviation in both grain size and porosity, a representation of grain size and porosity by vertical height and position may better represent the distribution of both data sets. Scatter matrices were created using the data set to confirm this hypothesis, with an example shown in Figure 4-20.

As shown, grain size shows a stronger dependence on vertical height rather than position, with more refined grain sizes near the base of the strip rather than the bulk and top of the strip.

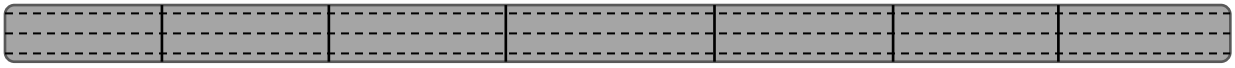

Figure 4-18 Cross-section of strip illustrating sampling for micro-property analysis, where the dotted lines represent the vertical height measurements and the solid lines represent the position sampling showing a sum of 7 samples

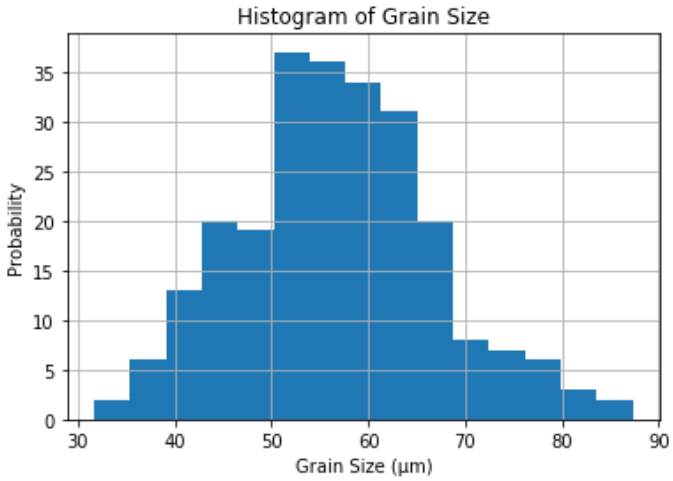

Figure 4-19 Histogram of Grain Size for 200 mm wide AA2024 strips

Table 4-3 Summary of Grain Size and Porosity Measurements in the HSBC Pilot-scale cast of AA2024

	Grain Size (180 mm wide strip)	Grain Size (200 mm wide strip)	Porosity (180 mm wide strip)	Porosity (200 mm wide strip)
Mean	53.9 µm	56.81 µm	1.43%	1.81%
Standard Deviation	9.36 µm	10.19 µm	0.79%	1.03%
Min	33.1 µm	31.7 µm	0.31%	0.25%
25%	46.68 µm	50.3 µm	0.86%	1.01%
50%	54.5 µm	56.5 µm	1.26%	1.56%
75%	60.5 µm	63.2 µm	1.90%	2.55%
Max	76.7 µm	87.3 µm	3.73%	4.10%

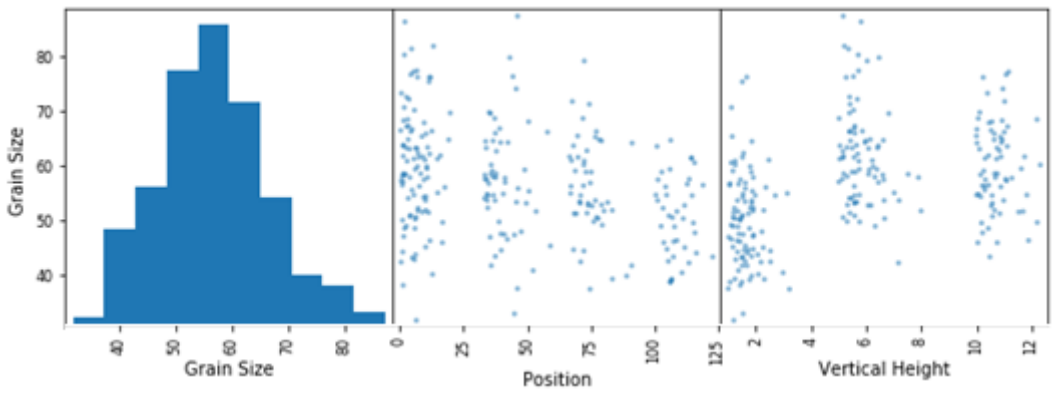

Figure 4-20 Scatter matrix between grain size, position and vertical height for 200 mm wide AA2024 strips

A summary of grain size and porosity measurements relative to position and vertical height are shown in Table 4-4, Table 4-5, Table 4-6, and Table 4-7. In terms of porosity, the relationship in both cases showed porosity significantly lower near the center of the strip relative to the edge of the strip. With regards to vertical height, the porosity near the center of the strip was shown to be the lowest in both cases, with the 200 mm wide strip showing significant improvement in the centre in comparison to the bottom and top of the strip.

Table 4-4 Grain size and porosity measurements depending on horizontal position for 180 mm wide strip

	Position: 0 mm	**Position: 30 mm**	**Position: 60 mm**	**Position: 90 mm**
Grain Size Mean	54.32 µm	53.68 µm	52.14 µm	50.12 µm
Grain Size Standard Deviation	7.29 µm	10.93 µm	9.63 µm	9.68 µm
Porosity Mean	1.74%	1.03%	0.99%	0.93%
Porosity Standard Deviation	0.78%	0.51%	0.54%	0.63%

Table 4-5 Grain size and porosity measurements depending on vertical height for 180 mm wide strip

	Vertical Height: 1 mm	Vertical Height: 4.15 mm	Vertical Height: 8.3 mm
Grain Size Mean	44.04 µm	58.93 µm	59.38 µm
Grain Size Standard Deviation	5.32 µm	5.60 µm	7.04 µm
Porosity Mean	1.43%	1.15%	1.50%
Porosity Standard Deviation	0.89%	0.60%	0.89%

Table 4-6 Grain size and porosity measurements depending on horizontal position for 200 mm wide strip

	Position: 0 mm	Position: 33.3 mm	Position: 66.6 mm	Position: 100 mm
Grain Size Mean	59.78 µm	57.23 µm	55.55 µm	52.56 µm
Grain Size Standard Deviation	10.62 µm	10.38 µm	8.66 µm	7.37 µm
Porosity Mean	2.21%	2.15%	1.55%	1.23%
Porosity Standard Deviation	1.06%	1.17%	0.88%	0.71%

Table 4-7 Grain size and porosity measurements depending on vertical height for 200 mm wide strip

	Vertical Height: 1 mm	**Vertical Height: 5 mm**	**Vertical Height: 10 mm**
Grain Size Mean	49.87 μm	62.00 μm	59.81 μm
Grain Size Standard Deviation	8.58 μm	9.19 μm	7.95 μm
Porosity Mean	2.01%	1.36%	1.98%
Porosity Standard Deviation	1.33%	0.61%	0.92%

Edited micrographs, as shown in Figure 4-21, displays the shrinkage porosity found in the 180 mm wide AA2024 strip. Shrinkage pores were shown to be scattered with irregular shapes throughout the strip, while circular pores caused by gas entrapment were rarer. The size of pores was measured with sizes primarily ranging from 20-200 μm in length.

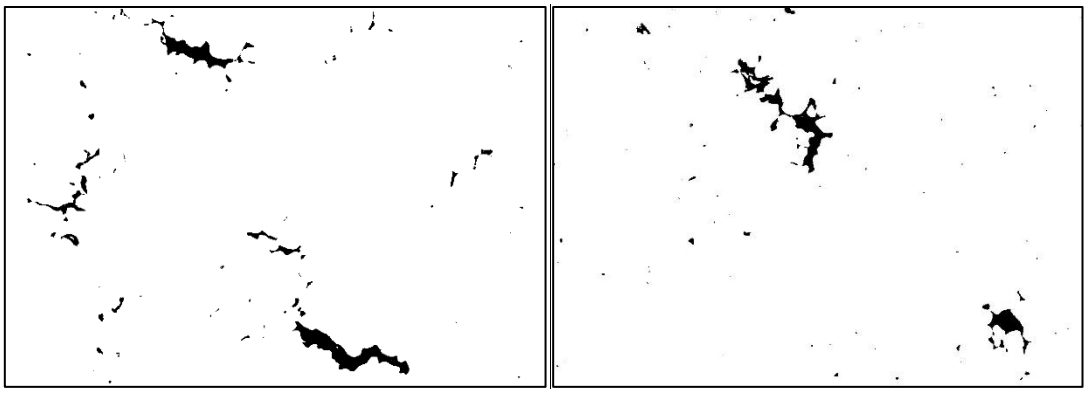

Figure 4-21 Edited micrographs showing typical porosity in 180 mm wide AA2024 strips (100X magnification)

With regards to microstructure, the grains were shown to be small and equiaxed throughout the strip, with no clear columnar grains existing in the transition from small to large equiaxed grains. It is clearly shown that grain sizes at the bottom surface of the strip were the most refined, while the bulk and the top of the strip exhibited very similar microstructure. This is due to the high heat transfer occurring at the bottom of the strip due to the water-cooled moving belt. The micrographs are shown in Figure 4-22, where the grains are distinct in size for the various vertical heights. With respect to traditional DC cast AA2024 with similar additions of titanium based refiners, where the grain sizes are in the range of 70 to 90 μm [50], it is clear that the HSBC process achieves a more refined microstructure, where grain sizes are in the range of 47 to 63 μm. This will reduce the sensitivity to hot cracking during casting as well as improve the mechanical properties of the as-cast material, at a much lower processing cost and much higher yield.

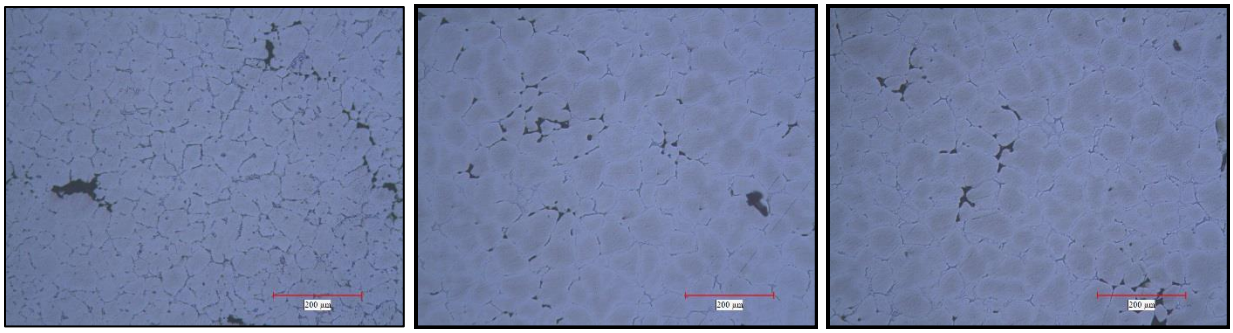

Figure 4-22 Micrographs at 100X magnification at the bottom of the strip (Left), the center of the strip (Middle) and the top of the strip (Right) for a 180 mm wide strip

A comparison of as-cast AA2024 produced by the HSBC process and by the DC casting process is shown in Figure 4-23. At the center of both as-cast AA2024 products, it is clear that the grains of HSBC cast AA2024 are small and equiaxed in comparison to the coarse grains present in DC cast AA2024.

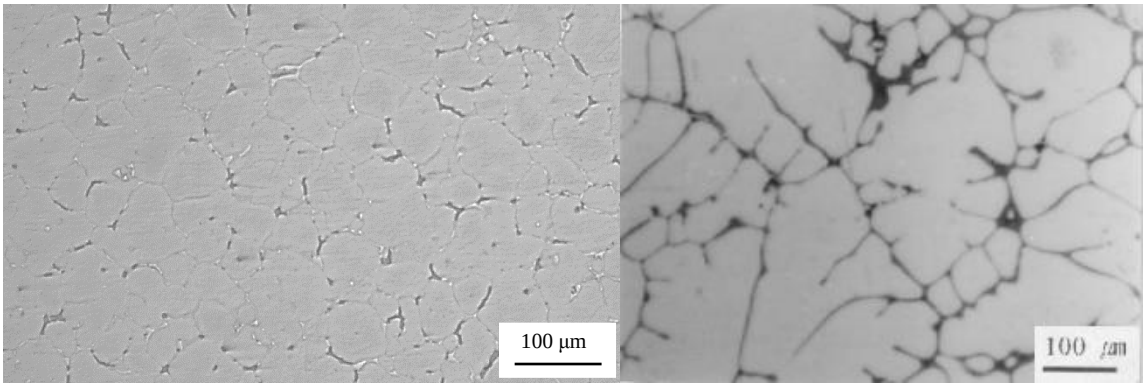

Figure 4-23 Optical micrographs at the center of as-cast AA2024 as produced by the HSBC process (Left) and by the DC process [95] (Right)

4.6 Mechanical Properties of as-cast AA2024 strips using the HSBC Pilot-scale machine

Vickers hardness value of 151 ± 7.2 was obtained using microhardness tests, showing improvement in comparison to the standard Vickers hardness of 137 for AA2024-T6 [96]. This increase is primarily due to the improved microstructure found in the HSBC produced AA2024 strip in comparison to those DC cast. Several shear punch test measurements were taken at various locations to ensure an accurate representation of the strip. Figure 4-24 shows a composite of the shear stress plots. Clear elastic and plastic deformation of the material is shown. Using the shear strain curves and equation (60), ultimate tensile strength and tensile yield strength were determined. A summary of the results is shown in Table 4-8 including a comparison to standard AA2024-T6. As expected, the material properties exhibited nearly identical tensile strength in comparison to AA2024-T6. Since the primary strength of the material lies in the copper precipitates, precipitation growth will have a significant impact on the material strength of AA2024. The current results show promise in the microstructure and mechanical properties. With additional heat treatment and rolling, it can be expected that the tensile behavior of HSBC produced AA2024 will be significantly improved in comparison to DC-cast AA2024.

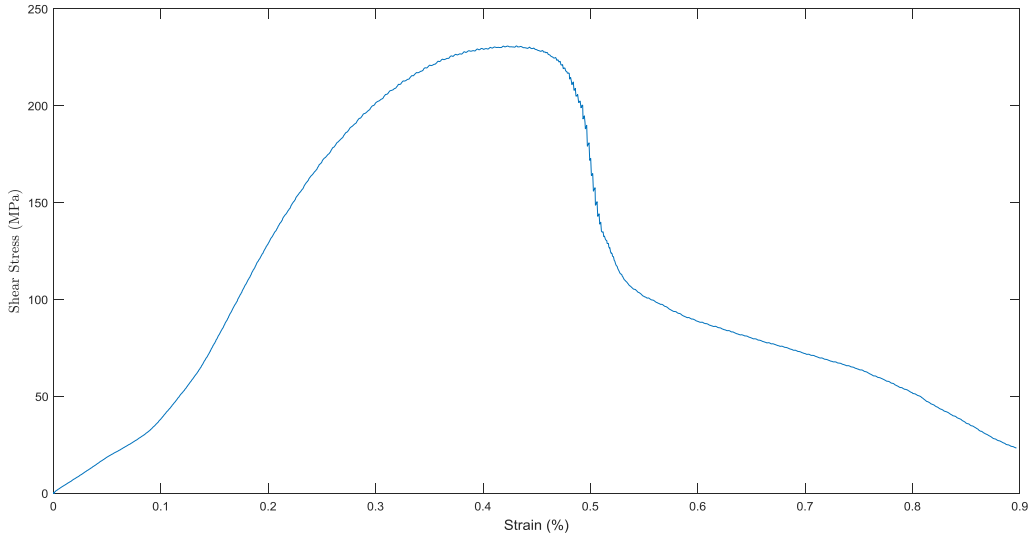

Figure 4-24 Shear stress vs Strain of as-cast AA2024 strip using the HSBC Pilot-scale machine

Table 4-8 Summary of HSBC produced as-cast AA2024 vs standard AA2024-T6

	HSBC produced as-cast AA2024	**AA2024-T6**
Hardness, Vickers	151	137
Ultimate Tensile Strength	426 MPa	427 MPa
Tensile Yield Strength	315 MPa	345 MPa

Chapter 5 Conclusions

From the present study, the following conclusions were made:

1. The transient CFD model showed an instability produced by the oscillating fluid flow at the first impingement. This was further confirmed by high speed videos previously produced at the McGill Metals Processing Centre showing edge flows and fluid instability.
2. By using the Kelvin Helmholtz Instability relationship, one can promote instability decay along the surface of the liquid melt and thus improve surface quality in the final product. This alongside the management of the Froude number at both impingements will improve surface quality and air entrapment within the liquid melt.
3. Simulator experiments showed heat fluxes of up to 11.8 MW/m^2 achieved in the casting of AA2024 strips, showing good agreement with previous experimental results and the numerical model.
4. 180 mm wide and 200 mm wide strips of AA2024 were successfully produced using the HSBC pilot-scale machine. Both strips exhibited excellent side quality and microstructure in comparison to traditional DC cast strips.
5. Surface quality was shown to dependent on the superheat of the liquid melt. With a higher superheat, the surface quality was shown to improve
6. Micro-properties like grain size and porosity was shown to have dependence on the position and vertical height within the strip. Porosity was found to be lower at the bulk of the strip in comparison to the edges. On the other hand, grain sizes were found to be the smallest at the bottom of the strip.
7. In comparison to traditional DC cast AA2024, the microstructure was shown to be more refined, indicating higher heat transfer rates. As a result, as-cast AA2024 showed similar tensile yield and ultimate strength in comparison to heat treated AA2024-T6 produced by DC cast.

Appendix I: Interfacial Heat Flux Analysis Code [59]

```
      CHARACTER ARQ*30,XIMP*30
      DOUBLE PRECISION A(2001),B(2001),C(2001),D(2001),T(2001),
     *TUSE0(2001),
     *Q1R(2001),QR(2001),TUSE1(2001),TUSE2(2001),TUSE3(2001),
     *TRT1(2001),qcomp(2001),
     *TRT2(2001),TIME(2001),POS(2001),K,Q2(2001),Q1(2001),C1,C2,
     *C3,CR,CC,DC
      REAL TIMEX(2001)
      WRITE(*,1047)

1047 FORMAT(5X,'ENTER THE NAMES OF THE FILES FOR :',/,8X,'- TEMPERATURE
     * READING ',//,8X,'- RESULTS : HEAT FLUX')
      READ(*,1048)ARQ

1048 FORMAT(A30)
      READ(*,1048)XIMP
      write(*,1048)ximp
      OPEN(8,FILE='PROP.DAT',STATUS='unknown')
      WRITE(*,629)

629  FORMAT(10X,'WHICH KIND OF COORDINATES DO YOU WANT TO USE ?',/,
     *15X,'[0]RECTANGULAR',/,15X,'[1]CYLINDRICAL',/,15X,'[2]ESPHERICAL'
     *)
      READ(*,*)S
      READ(8,*)RE,RI,CP,K,RO
      ENDFILE 8
      CLOSE(8,STATUS='KEEP')
      WRITE(*,1)RE,RI,CP,K,RO

1    FORMAT(10X,'PROPERTIES AND CHARACTERISTICS OF THE SYSTEM',//,10X,
     *'EXTERNAL RADIUS(M) = ',F7.5,/,10X,'INTERNAL RADIUS (M) = ',F7.5,
     */,10X,'SPECIFIC HEAT (J/KG.K) = ',F8.2,/,10X,'HEAT CONDUCTIVITY (
     *W/M.K.) = ',F8.2,/,10X,'DENSITY (KG/M3) = ',F8.2,//)

15   CONTINUE
      WRITE(*,2)

2    FORMAT(10X,'DO YOU WANT TO CHANGE ANY OF THESE DATA ? Y[1] N[2]')
      READ(*,*)ICH
      IF(ICH .EQ. 1)GOTO 3
      IF(ICH .EQ. 2)GOTO 4
      GOTO 15
```

```
3    WRITE(*,5)

5    FORMAT(10X,'ENTER THE PROPERTIES ABOVE IN THE SAME SEQUENCE AND SE
    *PARATED BY COMMA ')
     READ(*,*)RE,RI,CP,K,RO
     OPEN(8,FILE='PROP.DAT',STATUS='unknown')
     WRITE(8,*)RE,RI,CP,K,RO
     ENDFILE 8
     CLOSE(8,STATUS='KEEP')

4    CONTINUE
     WRITE(*,12)

12   FORMAT(/,10X,'ENTER THE NUMBER OF NODES N - UP TO 100')
     READ(*,*)N
     DO40I=1,N
     POS(I)=(FLOAT(I-1)*(RE-RI)/FLOAT(N-1)+RI)*1000.

40   CONTINUE
     WRITE(*,29)

29   FORMAT(10X,'SELECT THE POSITION OF THE SECOND THERMOCOUPLE',/,12X,
    *'ACCORDING TO THE FOLLOWING TABLE: ',/,10X,'NODE NUMBER-DISTANCE
    *TO THE CENTER')
     WRITE(*,41)(I,POS(I),I=1,N)

41   FORMAT(5(3X,I3,2X,F8.4))
     READ(*,*)NTC2
     WRITE(*,13)

13   FORMAT(/,10X,'ENTER THE NUMBER OF TEMPERATURE READINGS')
     READ(*,*)NREAD
     WRITE(*,6)

6    FORMAT(/,10X,'ENTER THE NUMBER OF TIME STEPS BETWEEN TWO READINGS'
    *)
     READ(*,*)NDIVT
     !OPEN(7,FILE='jason.txt',STATUS='unknown')
     OPEN(7,FILE=ARQ,STATUS='unknown')
     DO7 I=1,NREAD
     READ(7,*)TIME(I),TRT1(I),TRT2(I),QR(I)

7    CONTINUE
          ENDFILE 7
     CLOSE(7,STATUS='KEEP')
     DELTAR=(RE-RI)/FLOAT(N-1)
```

```
    ALFA=K/(RO*CP)
    DO600I=1,N
    T(I)=TRT1(1)+(TRT2(1)-TRT1(1))/(POS(NTC2)-POS(1))*(POS(I)-POS(1)
   *)

600  CONTINUE
    TUSE1(1)=T(NTC2-1)
    TUSE0(1)=T(NTC2-2)
    TUSE2(1)=T(NTC2)
    DO9999J=2,NREAD
    DELTAT=(TIME(J)-TIME(J-1))/FLOAT(NDIVT)
    DO9999JX=1,NDIVT
    JCONT=(J-2)*NDIVT+JX
    TIMEX(JCONT+1)=TIME(J-1)+FLOAT(JX)*DELTAT
    Q1R(JCONT+1)=QR(J)
    FO=ALFA*DELTAT/(DELTAR*DELTAR)
    B(1)=(TRT1(J)*FLOAT(JX)+TRT1(J-1)*FLOAT(NDIVT-JX))/FLOAT(NDIVT)
    C(1)=0.
    D(1)=1.
    DO 16 I=2,NTC2
    D(I)=1.+2.*FO
    R=FLOAT(I-1)*DELTAR+RI
    A(I-1)=FO*(-1.+S*DELTAR/(2.*R))
    C(I)=-FO*(1.+S*DELTAR/(2.*R))
    B(I)=T(I)
16   CONTINUE
    A(NTC2-1)=0.
    D(NTC2)=1.
    B(NTC2)=(TRT2(J)*FLOAT(JX)+TRT2(J-1)*FLOAT(NDIVT-JX))/FLOAT(NDIVT)
    CALL TRI(NTC2,A,D,C,B,T)
    TUSE2(JCONT+1)=T(NTC2)
    TUSE0(JCONT+1)=T(NTC2-2)
    TUSE1(JCONT+1)=T(NTC2-1)
9999 CONTINUE
    DO50IM=1,JCONT
    Q1(IM)=-K*(3.*TUSE2(IM)-4.*TUSE1(IM)+TUSE0(IM))/(2.*DELTAR)
50   CONTINUE
    DO2222I=NTC2,N-1
    JFIN=JCONT-(I-NTC2)-1
    DO1111JKK=2,JFIN
    JI=(JKK-2)/NDIVT+2
    JF=(JKK-1)/NDIVT+2
    DELTN=(TIME(JI)-TIME(JI-1))/FLOAT(NDIVT)
    DELTPO=(TIME(JF)-TIME(JF-1))/FLOAT(NDIVT)
    CC=DELTN/(DELTPO*(DELTN+DELTPO))
    DC=DELTPO/(DELTN*(DELTN+DELTPO))
```

```
      IF(S .NE. 0)GOTO 51
      CR=1.
      GOTO 52
51    CONTINUE
      CR=((RI+FLOAT(I-1)*DELTAR)/(RI+FLOAT(I)*DELTAR))**(S)
52    CONTINUE
      C1=DELTAR*CR/K
      C2=RO*CP*CR*DELTAR*DELTAR*CC/K
      C3=RO*CP*CR*DELTAR*DELTAR*DC/K
      Q2(JKK)=Q1(JKK)*CR-RO*CP*CR*DELTAR*(CC*(TUSE2(JKK+1)-TUSE2(JKK))-
     *DC*(TUSE2(JKK-1)-TUSE2(JKK)))
      TUSE3(JKK)=TUSE2(JKK)*(1.-C2+C3)-C1*Q1(JKK)+C2*TUSE2(JKK+1)-C3*TUS
     *E2(JKK-1)
1111  CONTINUE
      IF(I .EQ. N-1)GOTO 7777
      DO 555 JCA=2,JFIN
      TUSE2(JCA)=TUSE3(JCA)
      Q1(JCA)=Q2(JCA)
555   CONTINUE
2222  CONTINUE
7777  CONTINUE
      DO556JCA=2,JFIN
      Q2(JCA)=-Q2(JCA)
556   CONTINUE
      OPEN(15,FILE=XIMP,STATUS='unknown')
      DO 444 JCA=2,JCONT-(N-NTC2)
      WRITE(*,456)TIMEX(JCA),Q1R(JCA),Q2(JCA),TUSE3(JCA)
456   FORMAT(2X,F9.3,2X,2F14.2,2X,2F9.2)
      WRITE(15,456)TIMEX(JCA),Q1R(JCA),Q2(JCA),TUSE3(JCA)
444   CONTINUE
      ENDFILE 15
      CLOSE(15,STATUS='KEEP')
      END

      SUBROUTINE TRI(N,A,D,C,B,X)
      implicit DOUBLE PRECISION(a-h,o-z)
      dimension A(2001),D(2001),C(2001),B(2001),X(2001)
      DO2I=2,N
        XMULT=A(I-1)/D(I-1)
        D(I)=D(I)-XMULT*C(I-1)
        B(I)=B(I)-XMULT*B(I-1)
2     CONTINUE
      X(N)=B(N)/D(N)
      DO3I=N-1,1,-1
        X(I)=(B(I)-C(I)*X(I+1))/D(I)
3     CONTINUE
```

```
RETURN
END
```

Appendix II Python Script for Data Analysis of Micro-properties

```
#!/usr/bin/env python
# coding: utf-8

# In[1]:
import os
import matplotlib.pyplot as plt
import numpy as np
import pandas as pd
import random

# In[2]:
grain = r"Grainsize.csv"
porosity = r"porosity.csv"

# In[3]:
df_grain=pd.read_csv(grain)
df_porosity =pd.read_csv(porosity)

# In[4]:
df_grain.head(10)

# In[16]
:
fig = df_grain['Grain Size'].hist(bins=10)
plt.xlabel('Grain Size (μm)')
plt.ylabel('Probability')
plt.title('Histogram of Grain Size')
plt.grid(True)
plt.savefig('Histogram Grain Size.jpg')


# In[6]:
df_grain.groupby('Position').describe()


# In[7]:
df_grain.groupby('Vertical Height').describe()


# In[8]:
df_grain.describe()
```

```
# In[9]:
from pandas.plotting import scatter_matrix
scatter_matrix(df_grain,figsize=(10,10))
plt.savefig('Scatter Matrix Grain.jpg')

# In[10]:
fig = df_porosity['Porosity'].hist(bins=10)
plt.xlabel('Porosity')
plt.ylabel('Probability')
plt.title('Histogram of Porosity')
plt.grid(True)
plt.savefig('Histogram Porosity.jpg')

# In[11]:
df_porosity.groupby('Vertical Height').describe()

# In[12]:
df_porosity.groupby('Position').describe()

# In[13]:
df_porosity.describe()

# In[14]:
from pandas.plotting import scatter_matrix
scatter_matrix(df_porosity,figsize=(10,10))
plt.savefig('Scatter Matrix Porosity.jpg')
```

References

[1] R. I. Guthrie and J. G. Herbertson, "Continuous casting of thin metal strip," ed: Google Patents, 1990.

[2] R. I. L. Guthrie, M. Isac, and D. Li, "Ab-initio predictions of interfacial heat fluxes in horizontal single belt casting (HSBC), incorporating surface texture and air gap evolution," (in English), *ISIJ Int ISIJ International,* vol. 50, no. 12, pp. 1805-1813, 2010.

[3] W. Reichelt, K. Schwerdtfeger, and P. Voss-Spilker, "Apparatus for continuous casting," ed: Google Patents, 1988.

[4] S. Ge, "Numerical and physical modeling of the horizontal single belt casting (HSBC) process," (in English), 2016.

[5] R. I. L. Guthrie, "A review of fluid flows in liquid metal processing and casting operations," *ISIJ International,* vol. 49, no. 10, pp. 1453-1467, 2009.

[6] R. I. L. Guthrie, M. Isac, and D. Li, "Ab-initio Predictions of Interfacial Heat Flows during the High Speed Casting of Liquid Metals in Near Net Shape Casting Operations," (in English), *SRIN steel research international,* vol. 81, no. 10, pp. 891-898, 2010.

[7] R. I. L. Guthrie and M. Isac, "Horizontal single belt casting of aluminum and steel," *Steel Research International,* vol. 85, no. 8, pp. 1291-1302, 2014.

[8] D. Li, M. Isac, and R. Guthrie, "Improving Strip Surface Quality of AA6111 alloy using Different Casting Atmospheres for the Horizontal Single Belt Strip Casting (HSBC) Process," (in English), *Light metals.,* no. Year 2012, pp. 1101-1106, 2012.

[9] K.-H. Moon, "Physical and mathematical modeling of a metal delivery system for a single belt caster," McGill University Libraries, [Montreal], 2003.

[10] D. Li, J. Gill, M. Isac, and R. Guthrie, "Studies of Fluid Flow and Meniscus Behavior during Horizontal Single Belt Casting (HSBC) of Thin Metallic Strips," (in English), *Light metals.,* no. Year 2011, pp. 797-802, 2011.

[11] S. Ge, M. Isac, and R. I. L. Guthrie, "Progress in strip casting technologies for steel; Technical developments," *ISIJ international,* vol. 53, no. 5, pp. 729-742, 2013.

[12] M. M. Aboutalebi, "Mathematical and physical modeling of magnetic flow control in a vertical slot nozzle metal delivery system for a horizontal single belt caster," McGill University Libraries, [Montreal], 2015.

[13] S. Ge, M. Isac, and R. I. L. Guthrie, "The Computational Fluid Dynamic (CFD) Modeling of the Horizontal Single Belt Casting (HSBC) Processing of Al-Mg-Sc-Zr Alloy Strips," (in English), *Metall and Materi Trans B Metallurgical and Materials Transactions B,* vol. 46, no. 5, pp. 2264-2277, 2015.

[14] M. Xu, M. Isac, and R. I. L. Guthrie, "A Numerical Simulation of Transport Phenomena During the Horizontal Single Belt Casting Process Using an Inclined Feeding System," (in English), *Metall and Materi Trans B Metallurgical and Materials Transactions B,* vol. 49, no. 3, pp. 1003-1013, 2018.

[15] M. Xu, M. Isac, and R. I. L. Guthrie, "Transport phenomena during horizontal single belt casting process using an optimized inclined feeding system," *Ironmaking and Steelmaking*, 2018.

[16] M. Xu, M. Isac, and R. I. L. Guthrie, "Flow Instabilities in the Horizontal Single Belt Casting Process with an Inclined Feeding System," *ISIJ International*, 2018.

[17] S. Ge *et al.*, "Mathematical Modeling and Microstructure Analysis of Low Carbon Steel Strips Produced by Horizontal Single Belt Casting (HSBC)," (in English), *Metall and Materi Trans B Metallurgical and Materials Transactions B,* vol. 47, no. 3, pp. 1893-1904, 2016.

[18] J. Lee, M. Isac, and R. I. L. Guthrie, "Computational Study and Microstructural Analysis of AA2024 strips processed via the Horizontal Single Belt Casting Technique," presented at the Materials Science & Technology 2018, Columbus, Ohio, 2018.

[19] C.-H. Hsin, M. Isac, and R. I. L. Guthrie, "Numerical and Physical Modelling of Horizontal Single Belt Casting (HSBC) of AA55182 Alloy for the Production of Thin Strip Material," presented at the Materials Science & Technology 2018, Columbus, Ohio, 2018.

[20] U. Niaz, M. Isac, and R. I. L. Guthrie, "A Numerical Simulation of Tranport Phenomenon for the Casting of AA6111 Plate Using Horizontal Single Belt Pilot Caster," presented at the Materials Science & Technology 2018, Columbus, Ohio, 2018.

[21] J. Kim, "Interfacial heat transfer and solidfication of Mg and A1 alloys in a single belt casting process," McGill University Libraries, [Montreal], 2005.

[22] A. Changizi, M. Medraj, and M. Isac, "Effect of casting parameters on the microstructural and mechanical behavior of magnesium AZ31-B alloy strips cast on a single belt casting simulator," *Advances in Materials Science and Engineering*, vol. 2014, 2014.

[23] A. Changizi, "Effect of substrate material and roughness on the properties of Mg AZ31-B alloy cast on horizontal single belt casting simulator," Concordia University, 2009.

[24] M. Schäperkötter, H. Eichholz, J. Kroos, M. Niemeyer, R. Schmidt-Jürgensen, and K. Spitzer, "Direct Strip Casting (DSC)-an option for the production of HSD® steel grades," in *Proc. 1st. Int. Conf. on 'Super-high-strength steels', Rome, Italy*, 2005, pp. 188-199.

[25] S. Ge, M. Celikin, M. Isac, and R. I. L. Guthrie, "Mathematical Modeling and Microstructure Analysis of Al-Mg- Sc-Zr Alloy Strips Produced by Horizontal Single Belt Casting (HSBC)," *ISIJ International*, vol. 54, no. 2, pp. 294-303, 2014.

[26] D. Li, S. G. Shabestari, M. Isac, and R. I. Guthrie, "Studies in the Casting of AA6111 Strip on a Horizontal, Single Belt, Strip Casting Simulator," *TMS*, vol. 135, pp. 851-856, 2006.

[27] D. G, W. Yang, D. Yan, and L. Rong, "Hardening Behavior of the as-cast Al-Mg-Sc-Zr alloy," *Acta Metall Sin*, vol. 47, no. 3, pp. 311-316, 2011.

[28] M. Glazoff, V. Zolotorevsky, and N. Belov, *Casting Aluminum Alloys 1st Edition*. Elsevier, 2007.

[29] T. H. Muster, A. E. Hughes, and G. E. Thompson, "Copper distributions in aluminum alloys," (in English), 2009.

[30] J. L. Murray, "The aluminium-copper system," *International metals reviews,* vol. 30, no. 1, pp. 211-234, 1985.

[31] S. Wang and M. Starink, "Precipitates and intermetallic phases in precipitation hardening Al–Cu–Mg–(Li) based alloys," *International Materials Reviews,* vol. 50, no. 4, pp. 193-215, 2005.

[32] S. C. Wang, L. Chunzhi, B. Weimin, and B. W. Shuncai, "Microstructure study of constituent phases in 2024 series Al alloys," *Acta Metall Sin,* vol. 24, no. 5, pp. 30-35, 1989.

[33] E. Starke Jr and J. Staley, "Application of modern aluminum alloys to aircraft," *Progress in aerospace sciences,* vol. 32, no. 2-3, pp. 131-172, 1996.

[34] S. Wang, M. Starink, and N. Gao, "Precipitation hardening in Al–Cu–Mg alloys revisited," *Scripta Materialia,* vol. 54, no. 2, pp. 287-291, 2006.

[35] G. Sha, R. Marceau, X. Gao, B. Muddle, and S. Ringer, "Nanostructure of aluminium alloy 2024: Segregation, clustering and precipitation processes," *Acta Materialia,* vol. 59, no. 4, pp. 1659-1670, 2011.

[36] S. Wang and M. Starink, "The assessment of GPB2/S″ structures in Al–Cu–Mg alloys," *Materials Science and Engineering: A,* vol. 386, no. 1-2, pp. 156-163, 2004.

[37] R. K. Marceau, G. Sha, R. Ferragut, A. Dupasquier, and S. Ringer, "Solute clustering in Al–Cu–Mg alloys during the early stages of elevated temperature ageing," *Acta Materialia,* vol. 58, no. 15, pp. 4923-4939, 2010.

[38] Y. Lin, Y.-C. Xia, Y.-Q. Jiang, and L.-T. Li, "Precipitation in Al–Cu–Mg alloy during creep exposure," *Materials Science and Engineering: A,* vol. 556, pp. 796-800, 2012.

[39] C. G. Cordovilla and E. Louis, "Characterization of the microstructure of a commercial Al-Cu alloy (2 0 1 1) by differential scanning calorimetry (DSC)," *Journal of materials science,* vol. 19, no. 1, pp. 279-290, 1984.

[40] S. Ringer, T. Sakurai, and I. Polmear, "Origins of hardening in aged Al- Cu- Mg-(Ag) alloys," *Acta Materialia,* vol. 45, no. 9, pp. 3731-3744, 1997.

[41] M. Liu, S. Bai, Z. Liu, X. Zhou, P. Xia, and S. Zeng, "Analysis of modulus hardening in an artificial aged Al–Cu–Mg alloy by atom probe tomography," *Materials Science and Engineering: A,* vol. 629, pp. 23-28, 2015.

[42] M. Starink and S. Wang, "The thermodynamics of and strengthening due to co-clusters: general theory and application to the case of Al–Cu–Mg alloys," *Acta Materialia,* vol. 57, no. 8, pp. 2376-2389, 2009.

[43] A. Prasad and I. Bainbridge, "Experimental Determination of Heat Transfer Across the Metal/Mold Gap in a Direct Chill (DC) Casting Mold—Part I: Effect of Gap Size and Mold Gas Type," *Metallurgical and Materials Transactions A,* vol. 44, no. 1, pp. 456-468, 2013.

[44] D. G. Eskin, Physical metallurgy of direct chill casting of aluminum alloys, Boca Raton: CRC Press/Taylor & Francis, 2008. [Online]. Available.

[45] Q. Du, D. G. Eskin, and L. Katgerman, "Modeling Macrosegregation during Direct-Chill Casting of Multicomponent Aluminum Alloys," *Metallurgical and Materials Transactions A,* vol. 38, no. 1, pp. 180-189, 2007.

[46] M. M. Aboutalebi, M. Isac, and R. I. L. Guthrie, "A Study of the Effect of Rotary Electromagnetic Stirring on the Solidification Microstructure of Aluminum Alloys," presented at the Materials Science & Technology 2018, Columbus, Ohio, 2018.

[47] D. Eskin, "Effect of melt overheating on primary solidification in aluminium alloys," *Zeitschrift fur Metallkunde,* vol. 87, no. 4, pp. 295-299, 1996.

[48] S. Nikzad, H. Ashuri, A. Kokabi, M. Shafizadeh, and K. Ferasat, "Newly Developed Technique to Eliminate Hot Cracking with Electromagnetic Vibration for Joining of 2024 Aluminum Alloy," (in English), *Metallogr. Microstruct. Anal. Metallography, Microstructure, and Analysis : Application and Innovation for Metals, Alloys, and Engineered Materials,* vol. 5, no. 1, pp. 7-15, 2016.

[49] X. Tian and C. O. H. Battelle, "A hot-cracking mitigation technique for welding high-strength aluminum alloy," *Welding Journal (Miami),* vol. 79, no. 1, pp. 9s-17s, 2000.

[50] R. Nadella, D. Eskin, and L. Katgerman, "Effect of Grain Refinement on Structure Evolution,"Floating" Grains, and Centerline Macrosegregation in Direct-Chill Cast AA2024 Alloy Billets," *Metallurgical and materials transactions A,* vol. 39, no. 2, pp. 450-461, 2008.

[51] R. Nadella, D. G. Eskin, and L. Katgerman, "Role of grain refining in macrosegregation upon direct chill casting of AA 2024 round billet," in *Materials science forum*, 2006, vol. 519, pp. 1841-1846: Trans Tech Publ.

[52] R. K. Paramatmuni, K.-M. Chang, B. S. Kang, and X. Liu, "Evaluation of cracking resistance of DC casting high strength aluminum ingots," (in English), *MSA</cja:jid> Materials Science & Engineering A,* vol. 379, no. 1, pp. 293-301, 2004.

[53] S. V. Patankar, *Numerical heat transfer and fluid flow*. Washington; New York: Hemisphere Pub. Corp. ; McGraw-Hill, 1980.

[54] S. V. Patankar, "A calculation procedure for two-dimensional elliptic situations," *Numerical heat transfer,* vol. 4, no. 4, pp. 409-425, 1981.

[55] R. I. Issa, A. D. Gosman, and A. P. Watkins, "The computation of compressible and incompressible recirculating flows by a non-iterative implicit scheme," *Journal of Computational Physics,* vol. 62, no. 1, pp. 66-82, 1986.

[56] R. I. Issa, "Solution of the implicitly discretised fluid flow equations by operator-splitting," *Journal of Computational Physics,* vol. 62, no. 1, pp. 40-65, 1986.

[57] B. E. Launder and D. B. Spalding, "The numerical computation of turbulent flows," (in English), *Computer Methods in Applied Mechanics and Engineering,* vol. 3, no. 2, pp. 269-289, 1973.

[58] B. Launder, A. Morse, W. Rodi, and D. Spalding, "Prediction of free shear flows: a comparison of the performance of six turbulence models," 1973.

[59] R. Guthrie and R. Tavares, "Mathematical and physical modelling of steel flow and solidification in twin-roll/horizontal belt thin-strip casting machines," *Applied Mathematical Modelling,* vol. 22, no. 11, pp. 851-872, 1998.

[60] C. Jefferies, "Modelling a novel, thin strip, continuous steel caster delivery system," *rue,* vol. 1, p. 4, 1996.

[61] D. C. Wilcox, "Reassessment of the scale-determining equation for advanced turbulence models," *AIAA Journal,* vol. 26, no. 11, pp. 1299-1310, 1988.

[62] F. R. Menter, "Two-equation eddy-viscosity turbulence models for engineering applications," *AIAA journal,* vol. 32, no. 8, pp. 1598-1605, 1994.

[63] A. Jonayat and B. G. Thomas, "Transient thermo-fluid model of meniscus behavior and slag consumption in steel continuous casting," *Metallurgical and Materials Transactions B,* vol. 45, no. 5, pp. 1842-1864, 2014.

[64] C. Kratzsch, A. Asad, and R. Schwarze, "Comparison of different Methods to model Transient Turbulent Magnetohydrodynamic Flow in Continuous Casting Molds," in *IOP Conference Series: Materials Science and Engineering*, 2016, vol. 143, no. 1, p. 012025: IOP Publishing.

[65] K. Timmel, X. Miao, S. Eckert, D. Lucas, and G. Gerbeth, "Experimental and numerical modeling of the steel flow in a continuous casting mould under the influence of a transverse DC magnetic field," *Magnetohydrodynamics,* vol. 46, no. 4, pp. 337-448, 2010.

[66] X. Miao, K. Timmel, D. Lucas, Z. Ren, S. Eckert, and G. Gerbeth, "Effect of an electromagnetic brake on the turbulent melt flow in a continuous-casting mold," *Metallurgical and Materials Transactions B,* vol. 43, no. 4, pp. 954-972, 2012.

[67] K. Timmel *et al.*, "Experimental and numerical modelling of the fluid flow in the continuous casting of steel," *The European Physical Journal Special Topics,* vol. 220, no. 1, pp. 151-166, 2013.

[68] A. Pelss, A. Rueckert, and H. Pfeifer, "Numerical investigations of influences on the flow in a vertical twin roll strip caster for stainless steel," *METALLURGIA ITALIANA,* no. 2, pp. 29-34, 2016.

[69] M. N. Ozisik, "Inverse Heat Transfer : Fundamentals and Applications," (in English), 2017.

[70] D. W. Marquardt, "An algorithm for least-squares estimation of nonlinear parameters," *Journal of the society for Industrial and Applied Mathematics,* vol. 11, no. 2, pp. 431-441, 1963.

[71] Y. Bard, "Comparison of gradient methods for the solution of nonlinear parameter estimation problems," *SIAM Journal on Numerical Analysis,* vol. 7, no. 1, pp. 157-186, 1970.

[72] H. R. Busby and D. M. Trujillo, "Numerical solution to a two-dimensional inverse heat conduction problem," *International Journal for Numerical Methods in Engineering*, vol. 21, no. 2, pp. 349-359, 1985.

[73] C. H. Huang and M. N. Ozisik, "Optimal regularization method to determine the strength of a plane surface heat source," *International Journal of Heat and Fluid Flow*, vol. 12, no. 2, pp. 173-178, 1991.

[74] A. N. Tikhonov, "Regularization of incorrectly posed problems," in *Soviet Mathematics Doklady*, 1963, vol. 4, pp. 1624-1627.

[75] A. Tikhonov, "Inverse problems in heat conduction," *Journal of Engineering Physics and Thermophysics*, vol. 29, no. 1, pp. 816-820, 1975.

[76] J. V. Beck, B. Blackwell, and C. R. St. Clair, *Inverse heat conduction : ill-posed problems*. New York: Wiley, 1985.

[77] V. A. Morozov, Methods for Solving Incorrectly Posed Problems, New York, NY: Springer New York, 1984. [Online]. Available: http://dx.doi.org/10.1007/978-1-4612-5280-1.

[78] V. A. Morozov and M. Stessin, *Regularization methods for ill-posed problems*. CRC press Boca Raton, FL:, 1993.

[79] N. Zabaras, "Inverse problems in heat transfer," *Handbook of Numerical Heat Transfer*, pp. 525-557, 2006.

[80] K. Levenberg, "A method for the solution of certain non-linear problems in least squares," *Quarterly of applied mathematics*, vol. 2, no. 2, pp. 164-168, 1944.

[81] E. Polak, *Computational methods in optimization: a unified approach*. Academic press, 1971.

[82] R. Fletcher and C. M. Reeves, "Function minimization by conjugate gradients," *The computer journal*, vol. 7, no. 2, pp. 149-154, 1964.

[83] E.-Y. Ko, J. Choi, J.-Y. Park, and I. Sohn, "Simulation of low carbon steel solidification and mold flux crystallization in continuous casting using a multi-mold simulator," *Metals and Materials International*, vol. 20, no. 1, pp. 141-151, 2014.

[84] H. Zhang, W. Wang, D. Zhou, F. Ma, B. Lu, and L. Zhou, "A study for initial solidification of sn-pb alloy during continuous casting: Part I. The development of the technique," *Metallurgical and Materials Transactions B*, vol. 45, no. 3, pp. 1038-1047, 2014.

[85] H. Zhang, W. Wang, and L. Zhou, "Calculation of heat flux across the hot surface of continuous casting mold through two-dimensional inverse heat conduction problem," *Metallurgical and Materials Transactions B*, vol. 46, no. 5, pp. 2137-2152, 2015.

[86] M. Martorano and J. Capocchi, "Heat transfer coefficient at the metal–mould interface in the unidirectional solidification of Cu–8% Sn alloys," *International Journal of Heat and Mass Transfer*, vol. 43, no. 14, pp. 2541-2552, 2000.

[87] R. Parreiras Tavares, "Vertical twin-roll caster : metal-mould heat transfer, solidification and product characterization," McGill University Libraries, [Montreal], 1997.

[88] D. C. Wilcox, *Turbulence modeling for CFD*. La Cãnada, CA: DCW Industries, Inc., 1993.

[89] J. U. Brackbill, D. B. Kothe, and C. Zemach, "A continuum method for modeling surface tension," *Journal of Computational Physics,* vol. 100, no. 2, pp. 335-354, 1992.

[90] K. Bruno and M. J. McCready, "Origin of roll waves in horizontal gas-liquid flows," *AIChE Journal,* vol. 34, no. 9, pp. 1431-1440, 1988.

[91] M. Najafiyazdi, "Lecture 11: Instability and Transition," Lecture, 2018, 2018.

[92] B. Freeze, S. Smolentsev, N. Morley, and M. Abdou, "Characterization of the effect of Froude number on surface waves and heat transfer in inclined turbulent open channel water flows," *International Journal of Heat and Mass Transfer,* vol. 46, no. 20, pp. 3765-3775, 2003.

[93] E. J. F. R. Caron, A. R. Baserinia, H. Ng, M. A. Wells, and D. C. Weckman, "Heat-Transfer Measurements in the Primary Cooling Phase of the Direct-Chill Casting Process," *Metallurgical and Materials Transactions B,* vol. 43, no. 5, pp. 1202-1213, 2012.

[94] D. Li, M. Isac, and R. Guthrie, "The Direct Observation and Modeling of Metal Flows in the Meniscus Region of Horizontal Single Belt Strip Casting Process," *Roderick Guthrie Honary Symposium on Process Metallurgy,* 2011.

[95] S. W. Kim and H. Hao, "Microstructure and fatigue characteristics of direct chill cast and electromagnetic cast 2024 Al alloy ingots," *Metallurgical and Materials Transactions A,* vol. 34, no. 7, pp. 1537-1543, 2003.

[96] A.-A. S. M. Inc. *ASM Material Data Sheet Aluminum 2024-T6*.